Article

Neural control of affiliative touch in prosocial interaction

https://doi.org/10.1038/s41586-021-03962-w

Received: 21 January 2021

Accepted: 26 August 2021

Published online: 13 October 2021

Check for updates

Ye Emily Wu[1,2,3]✉, James Dang[1,2,3], Lyle Kingsbury[1,2], Mingmin Zhang[1,2], Fangmiao Sun[1,2], Rongfeng K. Hu[1,2] & Weizhe Hong[1,2]✉

The ability to help and care for others fosters social cohesiveness and is vital to the physical and emotional well-being of social species, including humans[1–3]. Affiliative social touch, such as allogrooming (grooming behaviour directed towards another individual), is a major type of prosocial behaviour that provides comfort to others[1–6]. Affiliative touch serves to establish and strengthen social bonds between animals and can help to console distressed conspecifics. However, the neural circuits that promote prosocial affiliative touch have remained unclear. Here we show that mice exhibit affiliative allogrooming behaviour towards distressed partners, providing a consoling effect. The increase in allogrooming occurs in response to different types of stressors and can be elicited by olfactory cues from distressed individuals. Using microendoscopic calcium imaging, we find that neural activity in the medial amygdala (MeA) responds differentially to naive and distressed conspecifics and encodes allogrooming behaviour. Through intersectional functional manipulations, we establish a direct causal role of the MeA in controlling affiliative allogrooming and identify a select, tachykinin-expressing subpopulation of MeA GABAergic (γ-aminobutyric-acid-expressing) neurons that promote this behaviour through their projections to the medial preoptic area. Together, our study demonstrates that mice display prosocial comforting behaviour and reveals a neural circuit mechanism that underlies the encoding and control of affiliative touch during prosocial interactions.

Helping and caring for others forms the ethos of our social lives—without these actions, we risk a loss of kinship, community and our own well-being. Among the wide diversity of social species, humans and other animals display prosocial behaviours, such as comforting, helping and resource sharing, to support the emotions, goals and/or material needs of other individuals[1–3]. While these behaviours are often driven by empathy, prosocial behaviours go beyond basic sensing and sharing of the affective states of other individuals by directing an active and targeted behavioural response to other individuals in need[1–3]. However, the neural mechanisms of how animals behave to help and benefit others remain largely unclear.

Affiliative social touch, such as allogrooming, serves as a common form of prosocial comforting behaviour that can provide a pleasant experience to others and often occurs in the context of consolation to alleviate stress in the recipient[3–6]. Allogrooming has a vital role in building and strengthening social bonds throughout a wide range of social species, such as birds, rodents, canids, equids and primates[3–6]. In humans, related forms of social touch—such as patting, caressing and hugging—tend to serve a similar function and are of vital importance to our social life[4,6]. However, little is known about the neural circuits that encode and promote affiliative touch during prosocial interactions.

Prosocial comforting behaviour in mice

In rodents, increased allogrooming towards distressed conspecifics has been observed in two monogamous vole species[7,8], but it is unclear whether mice exhibit allogrooming as a comforting behaviour. To examine whether mice display affiliative allogrooming in a prosocial context, we examined direct interactions between naive mice (subjects) and their co-housed partners that were subjected to a stressor (Fig. 1a and Methods). Interestingly, although subjects exhibited only occasional allogrooming towards unstressed partners, this behaviour was substantially increased towards distressed partners, with a longer duration and shorter onset latency (Fig. 1b–g, Extended Data Fig. 1a–f and Supplementary Video 1). This increase in allogrooming was observed in both male and female subjects (Extended Data Fig. 1a–f and Supplementary Note 1). By contrast, self-directed grooming did not increase during the same period (Fig. 1h and Extended Data Fig. 1g), arguing against a non-specific increase in generic grooming behaviour.

We also examined the behaviour displayed by stressed partners. These animals showed no increase in allogrooming compared with the separation-only control mice (Fig. 1i and Extended Data Fig. 1h) and their level of allogrooming was substantially lower compared with that of subjects (two-sided Wilcoxon signed-rank test, $P = 0.0001$ in males and $P = 0.0078$ in females). This suggests that allogrooming is a unidirectional

[1]Department of Biological Chemistry, David Geffen School of Medicine, University of California, Los Angeles, CA, USA. [2]Department of Neurobiology, David Geffen School of Medicine, University of California, Los Angeles, CA, USA. [3]These authors contributed equally: Ye Emily Wu and James Dang. ✉e-mail: ye.wu@ucla.edu; whong@ucla.edu

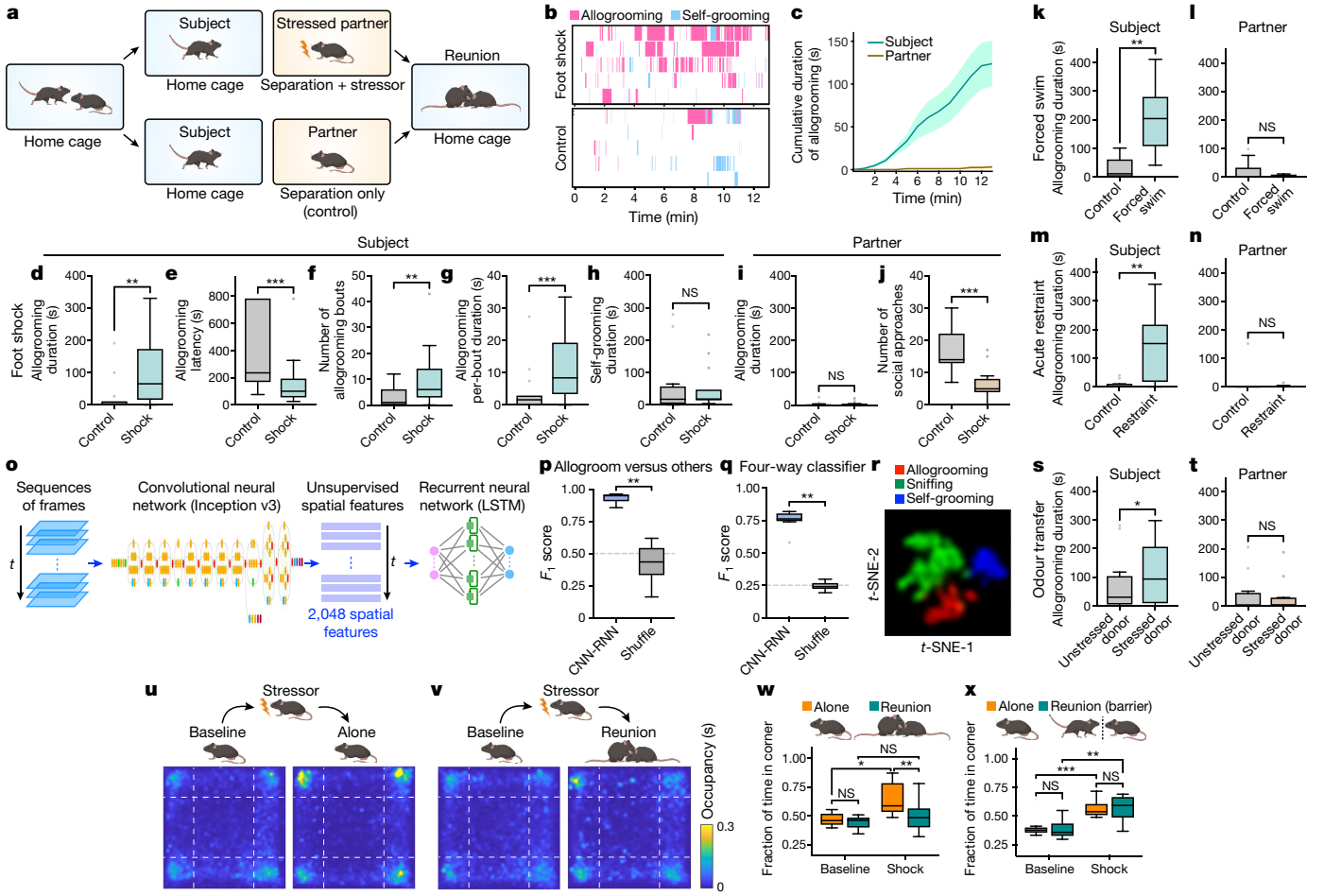

Fig. 1 | Mice display prosocial comforting behaviour. a, Schematic of the prosocial interaction assay. **b**, Example raster plots showing allogrooming and self-grooming during prosocial interaction. **c**, Time-course analysis of the cumulative allogrooming duration of subjects and partners after the partners experienced foot-shocks. Data are mean ± s.e.m. **d**–**h**, The total duration (**d**), onset latency (**e**), total bout number (**f**) and average per-bout duration (**g**) of allogrooming, and the total duration of self-grooming (**h**) exhibited by subjects interacting with unstressed (control) or foot-shocked partners. **i**, **j**, The total allogrooming duration (**i**) and the total number of social approaches towards subjects (**j**) exhibited by unstressed or foot-shocked partners. **k**–**n**, **s**, **t**, The total allogrooming duration of subjects (**k**, **m**, **s**) and partners (**l**, **n**, **t**) after the partners experienced forced swim (**k**, **l**) or acute restraint (**m**, **n**), or after odour transfer from a naive or stressed donor to partners (**s**, **t**). **o**, Schematic of the CNN-RNN framework for classifying behaviours. **p**, **q**, Performance of binary (**p**) and four-way multi-class (**q**) classification of allogrooming, sniffing, self-grooming or other behaviours. **r**, *t*-SNE visualization showing the separation of different behaviours on the basis of spatiotemporal features. **u**, **v**, Evaluation of the stress-relieving effect of prosocial interaction using the open field test. Partner mice either remained alone (**u**) or were reunited with subjects (**v**) after experiencing foot-shocks. The heat maps show partners' average occupancy at different locations. **w**, **x**, The fraction of time that partners spent in corners of the open field. Subject and partner mice either interacted freely (**w**) or were separated by a perforated barrier (**x**) during reunion. In **b**–**x**, the subjects are males; see Extended Data Fig. 1 for the female subjects. For the box plots in **d**–**n**, **p**, **q**, **s**, **t**, **w** and **x**, the centre line shows the median, the box limits show the quartiles, the whiskers show 1.5× the interquartile range (IQR), and the points show the outliers. ***$P < 0.001$, **$P < 0.01$, *$P < 0.05$. Details of the statistical analyses and sample sizes are provided in Supplementary Table 1.

behavioural response of subjects to stressed partners, as opposed to a general behavioural response to animals' own stress. Moreover, stressed partners exhibited a decrease in social approach towards subjects compared with controls (Fig. 1j and Extended Data Fig. 1i), suggesting that increased allogrooming by subjects was not solicited by stressed partners. Furthermore, we found no significant correlation between partners' self-grooming and subjects' allogrooming towards partners (Pearson correlation, $R^2 = 0.01$, $P = 0.79$), suggesting that increased allogrooming was probably not driven by partners' own self-grooming.

To determine whether increased allogrooming occurs in response to different types of stressors, we subjected partners to stressful experiences induced by forced swim or acute restraint procedures (Methods). Subjects, but not stressed partners, displayed a significant increase in allogrooming under both conditions (Fig. 1k–n), suggesting that the display of allogrooming can be generalized to different kinds of acute stressors (Supplementary Note 2).

We next examined whether allogrooming contains characteristic spatiotemporal features that can be reliably recognized using machine learning methods. We implemented a deep convolutional neural network (CNN) model (Google Inception v3) to extract unsupervised spatial features (as opposed to pose estimations), and used a LSTM-based recurrent neural network (RNN) to extract temporal features and classify behaviours in sequences of frames (Fig. 1o). Using this framework, allogrooming, sniffing and self-grooming events can be reliably classified (Fig. 1p, q and Extended Data Fig. 2a–f). To visualize the high-dimensional features in a semi-unsupervised manner, we performed *t*-distributed stochastic neighbour embedding (*t*-SNE) on the spatiotemporal features generated from the LSTM layer, and observed

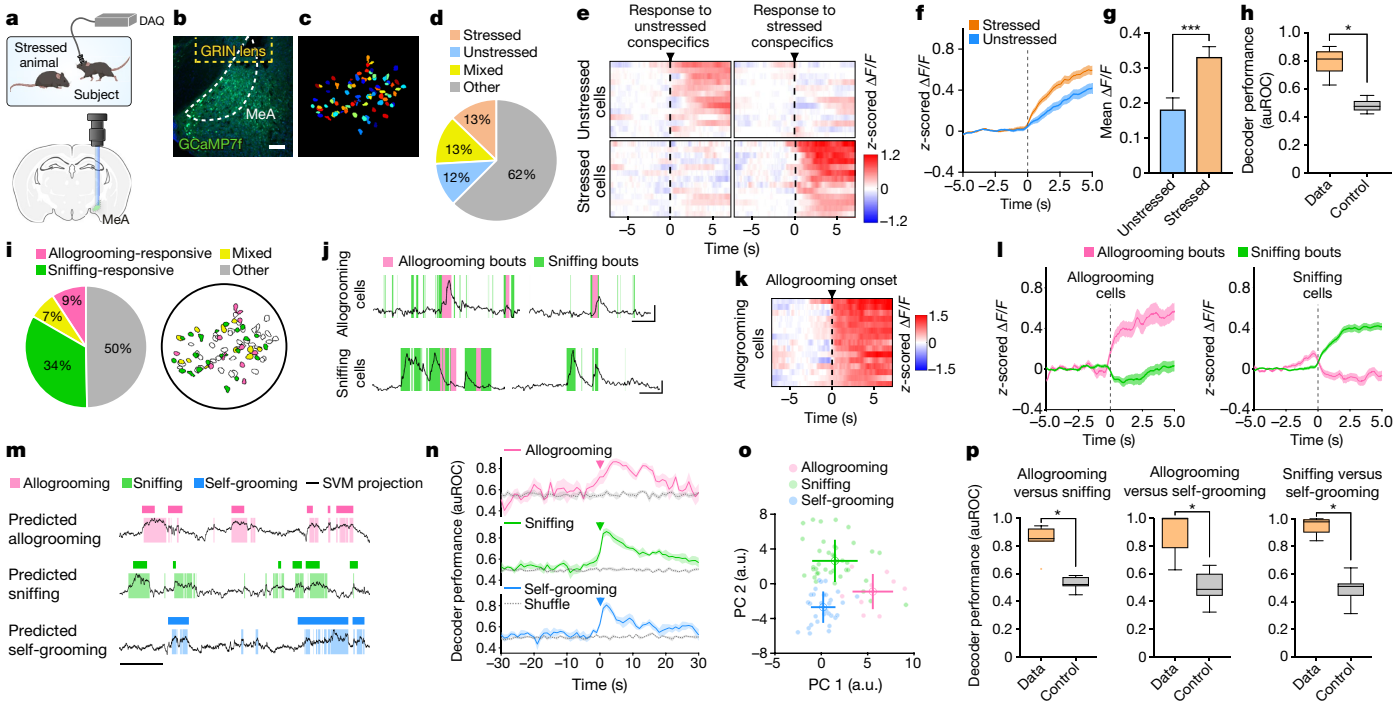

Fig. 2 | MeA neural dynamics during prosocial interaction. a, Schematic of microendoscopic imaging. **b**, Example image showing GCaMP7f expression in the MeA. GRIN, gradient refractive index. Scale bar, 100 µm. **c**, Single neurons extracted in an example field of view. **d**, The percentages of cells activated by unstressed and/or stressed conspecifics. **e**, The average responses of example cells activated specifically by unstressed or stressed conspecifics (but not both) aligned to the onset of sniffing towards different conspecifics. **f**, **g**, The responses of unstressed or stressed conspecific-activated (but not both-activated) MeA neurons during sniffing of unstressed or stressed animals, respectively (**f**), and mean $\Delta F/F$ (*z*-scored) during 0–3 s after the onset of sniffing (**g**). **h**, The performance of the decoder classification of sniffing towards unstressed versus stressed conspecifics using population activity. **i**, The percentages of cells that responded during allogrooming and/or sniffing and their spatial locations in an example field of view. **j**, Example calcium traces of allogrooming- and sniffing-activated cells showing increased single-neuron activity during allogrooming or sniffing towards stressed conspecifics. Scale bars, 40 s (horizontal) and 2σ $\Delta F/F$ (vertical). **k**, The average responses of example allogrooming-activated cells aligned to the onset of allogrooming. **l**, Average responses of allogrooming- and sniffing-activated cells during each behaviour. **m**, Decoder prediction of each behaviour using population activity overlaid with the ground truth. The plots show projections of population activity onto SVM (support vector machine) hyperplane, the dark patches show annotated behaviors (ground truth), and the light patches show predictions of decoders. Scale bar, 30 s. **n**, Time courses of decoder performance. **o**, Principal component projections of population activity associated with different behavioural events from one example session. The cross lines are mean ± s.d. **p**, The performance of decoders trained to discriminate between different behaviour pairs using population activity. Time 0 is the behaviour onset. For **f**, **g**, **l** and **n**, data are mean ± s.e.m. For the box plots in **h** and **p**, the centre line shows the median, the box limits show the quartiles, the whiskers show 1.5× the IQR, and the points show the outliers. ***$P < 0.001$, *$P < 0.05$. Details of the statistical analyses and sample sizes are provided in Supplementary Table 1.

an overall separation of allogrooming, sniffing and self-grooming (Fig. 1r). Thus, allogrooming is associated with characteristic spatiotemporal features that are separable from other social and non-social behaviours.

As olfactory cues emitted by stressed individuals can mediate the social transmission of stress in rodents[9], we examined whether olfactory cues also have a role in promoting allogrooming towards stressed partners. We transferred olfactory cues from a stressed donor mouse (or a naive donor as control) to a naive partner through an anogenital swab. Strikingly, odours transferred from stressed donors led to increased allogrooming by subjects towards partners compared with odours from naive donors (Fig. 1s), whereas allogrooming by partners showed no difference (Fig. 1t). This suggests that olfactory cues from stressed individuals can elicit allogrooming from other conspecifics.

Finally, we examined whether this interaction may generate a calming effect in stressed animals. The level of anxiety-associated behaviour of stressed partners reunited with subjects was significantly lower than that of the stressed partners that remained alone (Fig. 1u–w), suggesting that interaction with naive subjects produces a stress-reducing effect on stressed partners. We next performed a similar experiment but placed a perforated barrier between the animals during reunion (Methods). The presence of the divider abolished the stress-relieving effect, leading to similarly increased stress levels in foot-shocked partners in both the presence and absence of naive subjects (Fig. 1x). These data suggest that the mitigation of stress in partners requires close physical contact between the animals and is not merely due to the presence of naive subjects in the vicinity. Together, our findings indicate that mice display prosocial comforting behaviour towards distressed conspecifics.

Neural dynamics in prosocial interaction

The neural circuits that mediate adult-directed, affiliative social behaviour such as prosocial touch remain largely unknown[7,10]. The MeA is embedded in a highly connected social brain network and receives inputs from the olfactory system[11–18] (Extended Data Fig. 3i). Using in vivo microendoscopic calcium imaging, we recorded the neural activity of individual MeA neurons during free interaction with unstressed or stressed conspecifics (Fig. 2a–c and Supplementary Video 2). We found that subsets of MeA neurons showed significant responses to unstressed or stressed mice, with a fraction of them responding specifically to unstressed or stressed mice but not both (Fig. 2d, e). Moreover, neural responses towards unstressed and stressed animals could be

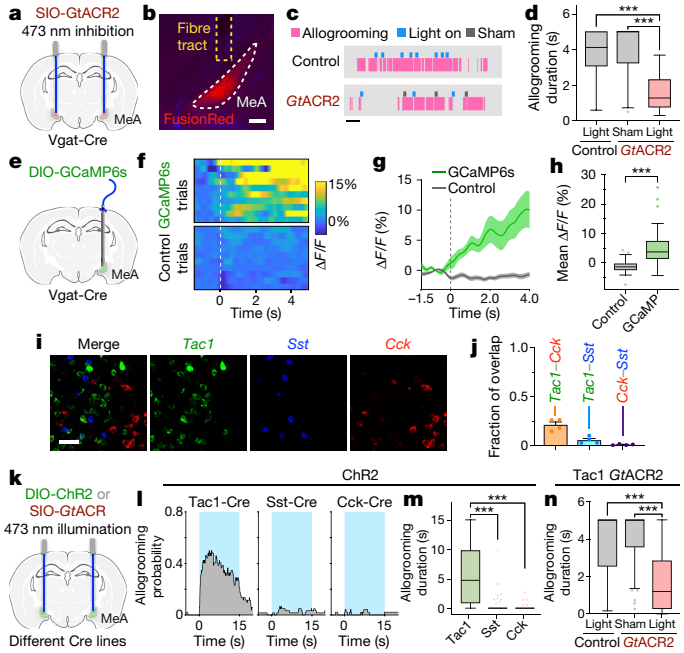

Fig. 3 | MeA^{Tac1} neurons underlie allogrooming. a, **e**, **k**, Schematics of *Gt*ACR2 inhibition (**a**), fibre photometry recording (**e**), and ChR2 activation and *Gt*ACR2 inhibition (**k**) in various MeA subpopulations. **b**, An example image showing *Gt*ACR2 expression in Vgat-Cre mice. Scale bar, 200 µm. **c**, **d**, Example raster plots (**c**) and duration (**d**) of allogrooming during real and sham photoinhibition (5 s) of MeA^{Vgat} neurons in control and *Gt*ACR2 animals. For **c**, scale bar, 20 s. **f**–**h**, Example heat maps (**f**) and average traces (**g**) showing Ca^{2+} signal changes aligned to allogrooming bouts and the mean $\Delta F/F$ after onset of allogrooming (**h**) in GCaMP or eYFP (enhanced yellow fluorescent protein) control animals. Time 0 is the onset of allogrooming. **i**, **j**, Expression of *Tac1*, *Sst* and *Cck* mRNA in the MeA (**i**) and overlaps between pairs of markers (**j**). Scale bar, 50 µm. **l**–**n**, Allogrooming probability (**l**) and duration (**m**, **n**) during activation (15 s) of MeA^{Tac1}, MeA^{Sst} and MeA^{Cck} neurons in ChR2 animals (**l**, **m**) and during real and sham photoinhibition (5 s) of MeA^{Tac1} neurons in control and *Gt*ACR2 animals (**n**). For **l**, the blue areas indicate the light illumination duration. Time 0 is the onset of illumination. For **g** and **j**, data are mean ± s.e.m. For the box plots in **d**, **h**, **m** and **n**, the centre line shows the median, the box limits show the quartiles, the whiskers show 1.5× the IQR, and the points show the outliers. ***$P < 0.001$. Details of the statistical analyses and sample sizes are provided in Supplementary Table 1.

decoded at the population level (Fig. 2h). Interestingly, neurons that are activated by stressed conspecifics showed a higher level of activity compared with neurons that are activated by unstressed conspecifics (Fig. 2f, g and Methods), indicating a different and stronger neural response to stressed conspecifics.

We next examined whether allogrooming is encoded by neural activity in the MeA. While 41% of MeA neurons significantly responded during sniffing behaviour (Fig. 2e, i, j, l and Extended Data Fig. 3b, d), 16% of MeA neurons showed significant responses during allogrooming, with 9% responding only to allogrooming but not sniffing (Fig. 2i–l and Extended Data Fig. 3a–d). Neurons that are specifically activated during allogrooming showed a minimal response during sniffing and vice versa (Fig. 2l), suggesting that activity changes in allogrooming-responsive neurons are not a general response to social sensory cues but contain an allogrooming-specific component. There is no anatomical clustering of allogrooming- or sniffing-responsive cells (Fig. 2i and Extended Data Fig. 3e). Although a fraction of neurons was active during self-grooming (Extended Data Fig. 3f, g), consistent with the role of MeA in self-grooming[17], these neurons showed no higher-than-chance overlap with those that are activated during allogrooming or sniffing (Extended Data Fig. 3h). Using linear decoders, we found that allogrooming, sniffing or self-grooming could each be predicted from population activity (Fig. 2m), with time courses that peaked during the execution of behaviour (Fig. 2n), suggesting that each behaviour is robustly encoded at the population level.

Finally, we examined whether the encoding of allogrooming in the MeA is distinct from the encoding of other behaviours that may involve similar sensory cues (sniffing) or motor patterns (self-grooming). Principal component analysis of neural responses during behaviour yielded components that separated different behaviour types (Fig. 2o and Extended Data Fig. 4a–d). We observed a similar separation of neural activity using deep-learning-based behaviour annotation (Extended Data Fig. 2g, h). Moreover, decoders constructed using population activity can discriminate between pairs of behaviours (Fig. 2p and Extended Data Fig. 4f–i), or between all three behaviour types (Extended Data Fig. 4e), suggesting that MeA neurons encode allogrooming, sniffing and self-grooming behaviours in distinct patterns of population activity. Interestingly, population activity around the onset of allogrooming could predict the duration of allogrooming (Extended Data Fig. 4j–n), suggesting a potential causal link between MeA activity and allogrooming behaviour.

MeA$^{Tac1 \cap Vgat}$ neurons drive allogrooming

GABAergic (Vgat$^+$) neurons in the MeA have important roles in social behaviour[13,17,18]. To determine whether these neurons are essential for native allogrooming, we first performed optogenetic inhibition using *Gt*ACR2 (*Guillardia theta* anion-conducting channelrhodopsin-2) during allogrooming towards stressed partners (Fig. 3a–d). Photoinhibition in *Gt*ACR2 animals led to a significant reduction in the duration of allogrooming in an acute, time-locked manner compared with sham or fluorescent protein controls (Fig. 3c, d and Methods). To determine whether MeA^{Vgat} neurons are active during natural allogrooming, we recorded Ca^{2+} dynamics in these neurons using fibre photometry (Fig. 3e). Indeed, MeA^{Vgat} neurons showed an elevated Ca^{2+} signal during allogrooming (Fig. 3f–h). These results support a functional requirement for MeA^{Vgat} neurons in natural allogrooming.

We next examined whether the regulation of allogrooming is a general function of the MeA^{Vgat} population as a whole or is mediated by one or more select subpopulations. Recent single-cell RNA-sequencing studies have uncovered the molecular profile of MeA GABAergic neurons[18]. These neurons express *Sst* (somatostatin), but not two other major GABAergic markers in the cortex, *Pvalb* and *Vip*[18]. Furthermore, they express several other neuropeptide genes, such as *Tac1* (tachykinin) and *Cck* (cholecystokinin)[18]. Here, we focused on three neuropeptide genes *Sst*, *Tac1* and *Cck*, which marked three neuronal subpopulations in the MeA with limited overlap (Fig. 3i, j and Supplementary Note 3).

Interestingly, optogenetic activation of the Tac1$^+$, but not the Sst$^+$ or Cck$^+$, population using ChR2 induced allogrooming in both males and females (Fig. 3k–m and Extended Data Fig. 5a–c, g, i–k, o), suggesting that MeA^{Tac1} neurons constitute a specific subpopulation that promotes allogrooming. Furthermore, *Gt*ACR2-mediated silencing of MeA^{Tac1} neurons caused a significant decrease in the duration of allogrooming compared with the controls (Fig. 3n), suggesting that activity of MeA^{Tac1} neurons is required for allogrooming.

Activation of MeA^{Tac1} neurons, but not the other subpopulations, also elicited self-grooming (Extended Data Fig. 5d–f, h, l–n, p). Previous studies showed that MeA glutamatergic neurons, but not GABAergic neurons, promote self-grooming[17]. Given that *Tac1* is also expressed in a subset of glutamatergic neurons in the MeA[18], we hypothesized that the glutamatergic subset of MeA^{Tac1} neurons mediates self-grooming, whereas GABAergic MeA^{Tac1} neurons promote allogrooming. To specifically target GABAergic MeA^{Tac1} neurons, we applied an intersectional approach wherein we expressed Cre- and Flp-dependent ChR2 (Con/Fon-ChR2) or eYFP (Con/Fon-eYFP) in Tac1-Cre/Vgat-Flp mice (Fig. 4a, d). We confirmed that Con/Fon-eYFP was expressed only in

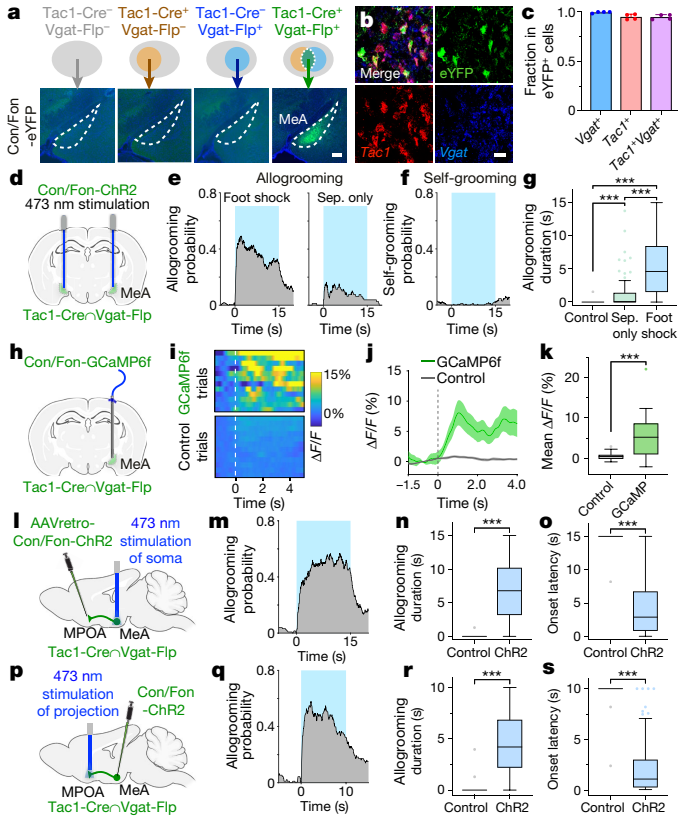

Fig. 4 | MPOA-projecting MeA$^{Tac1\cap Vgat}$ neurons drive allogrooming. **a**, Example images of Con/Fon-eYFP expression in the MeA of Tac1-Cre$^+$Vgat-Flp$^+$ (but not Tac1-Cre$^-$Vgat-Flp$^+$, Tac1-Cre$^+$Vgat-Flp$^-$ or Tac1-Cre$^-$Vgat-Flp$^-$) animals. Scale bar, 200 μm. **b**, **c**, Example images (**b**) and quantification (**c**) of the overlap between Tac1, Vgat and Con/Fon-eYFP expression in the MeA of Tac1-Cre$^+$Vgat-Flp$^+$ animals. Scale bar, 25 μm. **d**, **h**, **l**, **p**, Schematics of fibre photometry of MeA$^{Tac1\cap Vgat}$ neurons (**h**) and ChR2 activation of MeA$^{Tac1\cap Vgat}$ neurons (**d**), retrogradely targeted MPOA-projecting MeA$^{Tac1\cap Vgat}$ neurons (**l**), and axonal projections of MeA$^{Tac1\cap Vgat}$ neurons in the MPOA (**p**). **e**, **g**, The probability (**e**) and duration (**g**) of allogrooming towards foot-shocked or unstressed (sep. only) partners during photostimulation (15 s) in control and ChR2 animals. **f**, Self-grooming probability during photostimulation in ChR2 animals. **i**–**k**, Example heat maps (**i**) and average traces (**j**) showing Ca^{2+} signal changes aligned to allogrooming bouts and mean $\Delta F/F$ after onset of allogrooming (**k**) in GCaMP or eYFP control animals. Time 0 is the onset of allogrooming. **m**–**s**, The allogrooming probability (**m**, **q**), duration (**n**, **r**) and onset latency (**o**, **s**) during soma stimulation (15 s) of retrogradely targeted MPOA-projecting MeA$^{Tac1\cap Vgat}$ neurons (**m**–**o**) or stimulation (10 s) of axonal projections of MeA$^{Tac1\cap Vgat}$ neurons in the MPOA (**q**–**s**). For **e**, **f**, **m** and **q**, the blue areas show the stimulation duration. Time 0 is the stimulation onset. For **c** and **j**, data are mean ± s.e.m. For the box plots in **g**, **k**, **n**, **o**, **r** and **s**, the centre line shows the median, the box limits show the quartiles, the whiskers show 1.5× the IQR, and the points show the outliers. ***$P < 0.001$. Details of the statistical analyses and sample sizes are provided in Supplementary Table 1.

double-positive Tac1-Cre/Vgat-Flp mice but not in single-positive or double-negative mice (Fig. 4a), and that 95% of the cells expressing Con/Fon-eYFP were both Tac1 and Vgat positive (Fig. 4b, c). Consistent with our hypothesis, activating Tac1$^+$Vgat$^+$ MeA neurons (MeA$^{Tac1\cap Vgat}$ neurons) robustly induced allogrooming towards stressed partners in both male and female subjects, but did not elicit self-grooming (Fig. 4e–g, Extended Data Fig. 6a–g, Supplementary Video 3 and Supplementary Note 4). Although optogenetic stimulations in ChR2 subjects also induced allogrooming towards unstressed partners, the duration of allogrooming was longer when partners were stressed (Fig. 4e, g). These observations suggest that, similar to the increase in natural allogrooming towards stressed conspecifics, allogrooming elicited by optogenetic activation of MeA$^{Tac1\cap Vgat}$ neurons was elevated in the context of conspecific stress (Supplementary Note 5).

To confirm that glutamatergic MeA^{Tac1} neurons do not promote allogrooming, we adopted a Cre-on and Flp-off intersectional strategy wherein we expressed ChR2 primarily in Tac1$^+$Vgat$^-$ neurons (Extended Data Fig. 7a–c). Activation of these neurons indeed did not trigger allogrooming towards stressed partners but robustly elicited self-grooming (Extended Data Fig. 7d–f).

Finally, using fibre photometry, we found that MeA$^{Tac1\cap Vgat}$ neurons showed significantly increased activity during natural allogrooming (Fig. 4h–k). By contrast, Sst$^+$ neurons, which do not promote allogrooming, showed no overall increase in activity during allogrooming (Extended Data Fig. 5q, r). Together, these results identify a select subset of GABAergic neurons (Tac1$^+$Vgat$^+$) in the MeA that underlies allogrooming.

An MeA–MPOA circuit for allogrooming

To examine the downstream circuitry that regulates allogrooming, we examined the axonal projections of MeA$^{Tac1\cap Vgat}$ neurons and observed major projections to the medial preoptic area (MPOA; Extended Data Fig. 8a, b). To determine whether MPOA-projecting MeA$^{Tac1\cap Vgat}$ neurons have a role in driving allogrooming, we injected a retrograde virus expressing Con/Fon-ChR2 into the MPOA of Tac1-Cre/Vgat-Flp animals and implanted optic fibres above the MeA (Fig. 4l). Stimulating the somas of MPOA-projecting MeA$^{Tac1\cap Vgat}$ neurons led to time-locked induction of allogrooming towards stressed partners in both males and females (Fig. 4m–o, Extended Data Fig. 8c–g and Supplementary Note 4).

We next directly stimulated the axonal terminals of MeA$^{Tac1\cap Vgat}$ neurons in the MPOA by injecting a virus expressing Con/Fon-ChR2 into the MeA of Tac1-Cre∩Vgat-Flp animals and implanting optic fibres above the MPOA (Fig. 4p). This manipulation also elicited allogrooming in both males and females (Fig. 4q–s, Extended Data Fig. 8h–l, Supplementary Video 4 and Supplementary Note 4). It is unlikely that the evoked allogrooming was due to activation of collateral projections caused by antidromic activation of MeA somas, as inhibition of MeA cell bodies by intracranial infusion of lidocaine did not reduce the effect of photostimulating MPOA projections on allogrooming (Extended Data Fig. 8m–o). Furthermore, although the ventral premammillary nucleus (PMv) also receives projections from MeA$^{Tac1\cap Vgat}$ neurons (Extended Data Fig. 8p), stimulation of this projection produced a minimal effect on allogrooming (Extended Data Fig. 8q).

Previous studies show that the activation of MeA^{Vgat} neurons evokes attack behaviour towards intruder animals in a resident–intruder assay[17]. When light stimulation was delivered at lower intensities, activation of MeA^{Vgat} neurons could promote allogrooming towards distressed familiar partners without eliciting attack behaviour (Methods, Extended Data Fig. 9a–d and Supplementary Note 6). Interestingly, stimulation of MPOA-projecting MeA$^{Tac1\cap Vgat}$ neurons (Fig. 4l) did not promote any attack, even at high stimulation intensities. By contrast, activation of Tac1$^-$Vgat$^+$ neurons elicited substantial attack but minimal allogrooming towards stressed partners (Extended Data Fig. 10a–f and Supplementary Note 6). Together, our findings establish a primary role for MPOA-projecting MeA$^{Tac1\cap Vgat}$ neurons in promoting affiliative allogrooming.

Discussion

The ability to engage in prosocial behaviours that benefit others has important implications for the physical and emotional welfare of individuals and groups in humans and other animals. Although mice have been shown to exhibit social transmission of emotions such as fear and stress, direct physical interactions between bystanders and distressed

animals have rarely been studied[9,16,19–21]. By demonstrating that mice display prosocial comforting behaviour and identifying the MeA as a key node that encodes and drives this behaviour, our study provides an entry point for understanding how the MeA interacts with other brain areas that are involved in empathetic and prosocial processes, such as the anterior cingulate cortex[1,7,9,10,16,19–21] (Supplementary Note 7). Although the MeA was shown to regulate offspring-directed parenting behaviour[18], we demonstrate that it also has an essential role in a distinct social context (that is, adult-directed affiliative behaviour; Supplementary Note 8). How offspring- and adult-directed caring behaviours engage similar or distinct circuit mechanisms remains an interesting question for further investigations. Our finding that tachykinin-expressing MeA GABAergic neurons promote affiliative allogrooming through the MPOA reveals a previously unknown aspect of functional heterogeneity within MeA neurons and delineates a molecularly and anatomically defined circuitry that controls allogrooming. Given the role of the amygdala in prosocial decision-making in primates[22], our findings shed new light on how the amygdala regulates prosocial behaviour in different species. Insights from these investigations may impact our understanding of social cohesion and disconnection, such as in individuals experiencing neuropsychiatric conditions.

Online content

Any methods, additional references, Nature Research reporting summaries, source data, extended data, supplementary information, acknowledgements, peer review information; details of author contributions and competing interests; and statements of data and code availability are available at https://doi.org/10.1038/s41586-021-03962-w.

1. de Waal, F. B. M. & Preston, S. D. Mammalian empathy: behavioural manifestations and neural basis. *Nat. Rev. Neurosci.* **18**, 498–509 (2017).
2. Dunfield, K. A. A construct divided: prosocial behavior as helping, sharing, and comforting subtypes. *Front. Psychol* **5**, 958 (2014).
3. Rault, J.-L. Be kind to others: prosocial behaviours and their implications for animal welfare. *Appl. Anim. Behav. Sci.* **210**, 113–123 (2019).
4. Morrison, I. Keep calm and cuddle on: social touch as a stress buffer. *Adapt. Hum. Behav. Physiol.* **2**, 344–362 (2016).
5. Spruijt, B. M., Hooff, J. A. V. & Gispen, W. H. Ethology and neurobiology of grooming behavior. *Physiol. Rev.* **72**, 825–852 (1992).
6. Jablonski, N. G. Social and affective touch in primates and its role in the evolution of social cohesion. *Neuroscience* **464**, 117–125 (2020).
7. Burkett, J. P. et al. Oxytocin-dependent consolation behavior in rodents. *Science* **351**, 375–378 (2016).
8. Li, L.-F. et al. Involvement of oxytocin and GABA in consolation behavior elicited by socially defeated individuals in mandarin voles. *Psychoneuroendocrinology* **103**, 14–24 (2019).
9. Sterley, T.-L. & Bains, J. S. Social communication of affective states. *Curr. Opin. Neurobiol.* **68**, 44–51 (2021).
10. Paradiso, E., Gazzola, V. & Keysers, C. Neural mechanisms necessary for empathy-related phenomena across species. *Curr. Opin. Neurobiol.* **68**, 107–115 (2021).
11. Kwon, J.-T. et al. An amygdala circuit that suppresses social engagement. *Nature* **593**, 114–118 (2021).
12. Chen, P. & Hong, W. Neural circuit mechanisms of social behavior. *Neuron* **98**, 16–30 (2018).
13. Raam, T. & Hong, W. Organization of neural circuits underlying social behavior: a consideration of the medial amygdala. *Curr. Opin. Neurobiol.* **68**, 124–136 (2021).
14. Unger, E. K. et al. Medial amygdalar aromatase neurons regulate aggression in both sexes. *Cell Rep.* **10**, 453–462 (2015).
15. Li, Y. et al. Neuronal representation of social information in the medial amygdala of awake behaving mice. *Cell* **171**, 1176–1190 (2017).
16. Twining, R. C., Vantrease, J. E., Love, S., Padival, M. & Rosenkranz, J. A. An intra-amygdala circuit specifically regulates social fear learning. *Nat. Neurosci.* **20**, 459–469 (2017).
17. Hong, W., Kim, D.-W. & Anderson, D. J. Antagonistic control of social versus repetitive self-grooming behaviors by separable amygdala neuronal subsets. *Cell* **158**, 1348–1361 (2014).
18. Chen, P. B. et al. Sexually dimorphic control of parenting behavior by the medial amygdala. *Cell* **176**, 1206–1221 (2019).
19. Allsop, S. A. et al. Corticoamygdala transfer of socially derived information gates observational learning. *Cell* **173**, 1329–1342 (2018).
20. Jeon, D. et al. Observational fear learning involves affective pain system and $Ca_v1.2$ Ca^{2+} channels in ACC. *Nat. Neurosci.* **13**, 482–488 (2010).
21. Sterley, T.-L. et al. Social transmission and buffering of synaptic changes after stress. *Nat. Neurosci.* **21**, 393–403 (2018).
22. Gangopadhyay, P., Chawla, M., Monte, O. D. & Chang, S. W. C. Prefrontal–amygdala circuits in social decision-making. *Nat. Neurosci.* **24**, 5–18 (2021).

Methods

Mice

For characterization of prosocial interaction in wild-type mice, C57BL/6J male and female mice were first purchased from Jackson Laboratories (000664) and crossed to generate a breeding colony. Mice from this colony (aged 12–16 weeks) were used for behavioural experiments. C57BL/6J male mice purchased from Jackson Laboratories (000664) were used for microendoscopic calcium imaging experiments. For optogenetic and fibre photometry experiments, the following Cre and Flp driver lines were used: *Vgat*$^{cre/+}$, *Vgat*$^{flp/+}$, *Tac1*$^{cre/+}$, *Sst*$^{cre/+}$ and *Cck*$^{cre/+}$. All genotypes were first purchased from Jackson Laboratories (028862, 029591, 021877, 013044 and 012706) and backcrossed to C57BL/6J to generate a breeding colony. *Vgat*$^{flp/+}$ and *Tac1*$^{cre/cre}$ mice were crossed to generate *Vgat*$^{flp/+}$; *Tac1*$^{cre/+}$ mice. BALB/cJ male and female mice were purchased from Jackson Laboratories (000651). Animals used for stereotaxic surgery were aged 10–12 weeks. Animals were housed under a 12 h–12 h light–dark cycle (22:00–10:00 light), with food and water available ad libitum. The housing facility had a temperature of 21–23 °C and a humidity of 30–70%. All experiments were performed during the dark cycle of the animals in a dark room illuminated by infrared or red light. Care and experimental manipulations of all animals were carried out in accordance with the NIH Guide for Care and Use of Laboratory Animals and approved by UCLA IACUC.

Viruses

AAV1-hSyn1-SIO-stGtACR2-FusionRed (105677-AAV1), AAV1-syn-jGCaMP7f-WPRE (104488-AAV1), AAV1-syn-FLEX-jGCaMP7f-WPRE (104492-AAV1), AAVretro-hSyn-Con/Fon-hChR2-eYFP (55645-AAVrg), AAV5-EF1α-Con/Fon-GCaMP6f (137122-AAV5) and AAVretro-hSyn-HI.EGFP-Cre-WPRE (105540-AAVrg) were purchased from Addgene. AAV5-EF1α-DIO-GCaMP6s, AAV2-EF1α-DIO-hChR2(H134R)-eYFP, AAV5-hSyn-Con/Fon-hChR2(H134R)-eYFP, AAV5-hSyn-Con/Foff-hChR2-eYFP, AAV5-hSyn-Coff/Fon-hChR2(H134R)-eYFP, AAV2-EF1α-FLEX-mCherry, AAV2-EF1α-DIO-eYFP, AAV5-hSyn-Con/Fon-eYFP, AAV5-hSyn-Con/Foff-eYFP and AAV5-hSyn-Coff/Fon-eYFP were purchased from the University of North Carolina vector core. AAV2-EF1α-FLEX-ChR2-nuclear hrGFP was purchased from the University of Pennsylvania vector core.

Stereotaxic surgeries

Mice (aged 10–12 weeks) were anaesthetized with isoflurane and mounted on a stereotaxic device (Kopf instruments). Injections were performed using a pulled, fine glass capillary (WPI). The anatomical coordinates of the MeA were determined based on Paxinos and Franklin's *The Mouse Brain in Stereotaxic Coordinates* atlas and previous anatomical studies[23,24].

For optogenetic activation and inhibition of MeA cell bodies, viruses were injected bilaterally at ML (medial–lateral) ±2.15, AP (anterior–posterior) −1.55, DV (dorsal–ventral) −5.25 from bregma. Ferrule fibre-optic cannulas (200 μm core diameter, 0.37 numerical aperture; Inper) were placed 0.5 mm above the virus injection sites in the MeA. The type and volume of viruses injected at each site for different experiments were as follows: 400 nl AAV1-hSyn1-SIO-stGtACR2-FusionRed[25] (*Gt*ACR2 inhibition in *Vgat*$^{cre/+}$ mice); 450 nl AAV1-hSyn1-SIO-stGtACR2-FusionRed (*Gt*ACR2 inhibition in *Tac1*$^{cre/+}$ mice); 300 nl AAV2-EF1α-FLEX-ChR2-nuclear hrGFP (ChR2 activation in *Tac1*$^{cre/+}$ mice); 350–450 nl AAV2-EF1α-DIO-hChR2(H134R)-eYFP (ChR2 activation in *Sst*$^{cre/+}$ and *Cck*$^{cre/+}$ mice); 400 nl AAV5-hSyn-Con/Fon-hChR2(H134R)-eYFP[26], 450 nl AAV5-hSyn-Con/Foff-hChR2(H134R)-eYFP[26] or 300 nl AAV5-hSyn-Coff/Fon-hChR2(H134R)-eYFP[26] (ChR2 activation in *Vgat*$^{flp/+}$; *Tac1*$^{cre/+}$ mice); 200–250 nl AAV2-EF1α-FLEX-ChR2-nuclear hrGFP (ChR2 activation in *Vgat*$^{cre/+}$ mice).

For optogenetic activation of the MeA-to-MPOA projection, AAV5-hSyn-Con/Fon-hChR2(H134R)-eYFP was injected bilaterally into the MeA (ML ±2.15, AP −1.55, DV −5.25 from bregma) of *Vgat*$^{flp/+}$; *Tac1*$^{cre/+}$ mice with 450 nl at each site. Ferrule fibre-optic cannulas (200 μm core diameter, 0.37 numerical aperture; Inper) were then placed above the MPOA (left side, ML −0.4, AP 0.1, DV −4.75 from bregma; right side, angled 6°, ML 1.0, AP 0.1, DV −4.85 from bregma). For activation of the MeA-to-MPOA projection with inhibition of MeA cell bodies, AAV5-hSyn-Con/Fon-hChR2-eYFP was injected into the MeA as described above and a ferrule fibre-optic cannula was implanted unilaterally into the MPOA (ML 0.65, AP 0.15, DV −5.1 from bregma, angled 12°). A 26-gauge guide cannula for lidocaine injection was implanted above the ipsilateral MeA (ML −2.15, AP −1.55, DV −5.1 from bregma). For activation of the MeA-to-PMv projection, AAV5-hSyn-Con/Fon-hChR2(H134R)-eYFP was injected bilaterally into the MeA (ML ±2.15, AP −1.55, DV −5.25 from bregma) of *Vgat*$^{flp/+}$; *Tac1*$^{cre/+}$ mice with 500 nl at each site. Ferrule fibre-optic cannulas (200 μm core diameter, 0.37 numerical aperture; Inper) were then placed above the PMv (left side, ML −0.5, AP −2.4, DV −5.1 from bregma; right side, angled 6°, ML 1.05, AP −2.4, DV −5.25 from bregma).

For retrograde targeting of MPOA-projecting MeA neurons for ChR2 activation, AAVretro-hSyn-Con/Fon-hChR2-eYFP was injected bilaterally into the MPOA (ML ±0.45, AP 0.1, DV −4.85 from bregma) of *Vgat*$^{flp/+}$; *Tac1*$^{cre/+}$ mice with 500 nl at each site. Ferrule fibre-optic cannulas (200 μm core diameter, 0.37 numerical aperture; Inper) were then placed above the MeA (ML ±2.15, AP −1.55, DV −4.75 from bregma).

In optogenetic experiments, to avoid situations in which the baseline stress level of subject animals was substantially different from that of partner animals due to surgical procedures, we performed surgical procedures on both animals in a pair. In some pairs, partner animals received sham surgery but not fibre implantation and, in other pairs, partner animals also received fibre implantation. We did not observe any obvious difference in the effect of optogenetic manipulations in subject animals under these two conditions.

In the fibre photometry experiments, AAV5-EF1α-DIO-GCaMP6s[27] and AAV1-syn-FLEX-jGCaMP7f-WPRE[28] were injected bilaterally into the MeA (ML ±2.15, AP −1.55, DV −5.25 from bregma) of *Vgat*$^{cre/+}$ and *Sst*$^{cre/+}$ mice, respectively, with 250 nl at each site. AAV5-EF1a-Con/Fon-GCaMP6f[27] was injected bilaterally into the MeA (ML ±2.15, AP −1.55, DV −5.25 from bregma) of *Vgat*$^{flp/+}$; *Tac1*$^{cre/+}$ mice, with 400 nl at each site. Ferrule fibre-optic cannulas (200 μm core diameter, 0.37 numerical aperture; Inper) were implanted 0.2 mm above the injection site.

For microendoscopic calcium imaging, AAV1-syn-jGCaMP7f-WPRE[28] was injected unilaterally into the MeA at two sites (ML 2.15, AP −1.5 and −1.65, DV −5.3 from bregma) of C57BL/6J mice, with 300 nl at each site. A 0.6 mm (diameter) gradient refractive index (GRIN) lens (6 mm; Inscopix) was implanted above the injection site at ML 2.15, AP −1.6, DV −5.25 from bregma. After three weeks, a base plate was placed on top of the lens. Mice were individually housed after surgery.

For retrograde tracing of the AOB–MeA projection, 250 nl AAVretro-hSyn-HI.EGFP-Cre-WPRE was injected unilaterally into the MeA (ML 2.15, AP −1.55, DV −5.25 from bregma) of C57BL/6J mice.

For examining the expression patterns of Con/Fon-eYFP, Con/Foff-eYFP and Coff/Fon-eYFP in the MeA, 400 nl AAV5-hSyn-Con/Fon-eYFP or 300 nl AAV5-hSyn-Con/Foff-eYFP or AAV5-hSyn-Coff/Fon-eYFP was injected bilaterally into the MeA (ML ±2.15, AP −1.55, DV −5.25 from bregma) of *Vgat*$^{flp/+}$; *Tac1*$^{cre/+}$ mice.

All control animals in this study were animals with the same genetic background injected with eYFP- or mCherry-expressing AAVs.

Proper viral expression and fibre placement in brain areas of interest were confirmed post hoc using histology for all experiments.

Finally, in previous literature, the MeA was divided into four anatomical subdivisions: anterodorsal, anteroventral, posterodorsal (MeApd) and posteroventral subdivisions. With the stereotaxic coordinates used for viral injection in the MeA in the current study (ML ±2.15, AP −1.55, DV −5.25 from bregma), the labelled neurons were predominantly in the MeApd (Figs. 2b, 3b and 4a). The MeApd is outlined in Figs. 2b, 3b and

4a. Although different MeA subregions have overall different circuit connectivity and cytoarchitecture[13], the precise and definitive spatial boundaries between them have not been well-defined (particularly between the anterior and posterior subdivisions). While the effects of our optogenetic stimulations were primarily attributable to neurons in the MeApd, it remains possible that some neurons in the other subdivisions may also be involved in allogrooming behaviour.

Prosocial interaction assays

Prosocial interaction after foot shock. To examine prosocial interactions between mice, we adapted a paradigm that was previously used in prairie voles[7]. Same-sex pairs of male and female C57BL/6J mice were co-housed for at least 5 weeks before behavioural testing. Pairs of same-sex, co-housed familiar cage mates with small weight differences were used to minimize antagonistic, reproductive and/or novelty-driven interactions. One animal was randomly assigned as the subject and the other as the partner. The weight difference between the two mice in each pair was <4% for males and <12% for females. Before behavioural testing, the animals were extensively habituated to human handling procedures and to the behaviour set-up for at least three consecutive days. This habituation procedure is important for minimizing the potential influence of stress in subject animals caused by experimental procedures. For the separation-only test (control), the partner was removed from the home cage and placed into a separate cage with beddings from the home cage. After ~12 min, the partner was returned to the home cage to reunite with the subject. For the separation + stressor test, the partner was separated from the subject and transferred to a foot-shock chamber (Med Associates) in a separate room. The partner then received 20 foot shocks (0.7 mA, 1 s) with a random interval between 20 and 40 s, before being returned to the home cage. Post-separation/stressor behaviour was recorded for 13 min. Control experiments (separation-only test) were performed one day before the stress experiments. Behavioural testing was performed in the animals' home cage to avoid potential stress and/or novelty-related behaviours associated with new environments. The home cage was covered by a cage lid throughout the experiment whenever possible to minimize any perturbations from the environment. All of the experiments were performed during the dark cycle of the animals in a dark room illuminated by infrared or red light.

We also examined allogrooming behaviour after longer separation (2 h) of unstressed partners and found that there was no significant difference in the total duration of allogrooming by subject animals between 10 min and 2 h separation groups ($n = 10$ pairs of male mice; mean ± s.e.m., 10.5 ± 7.9 s (10 min separation), 27.3 ± 13.8 s (2 hour separation); two-sided Wilcoxon signed-rank test, $P = 0.2031$).

Videos from the experiments were manually annotated for different behaviours in a frame-by-frame manner using custom MATLAB code (https://github.com/pdollar/toolbox). Allogrooming was defined as visible licking and/or mouth contact localized on the body trunk, shoulder region and head of another mouse, during which the actor mouse shows head bobbing indicative of licking motions and frequently holds the recipient with forelimbs for stability (Supplementary Video 1). For the quantification of allogrooming bout number and bout duration, consecutive bouts with <1 s interval between them were considered to be one continuous bout. We did not observe barbering (characterized by a type of abnormal, repetitive grooming behaviour directed at self or cagemates, involving the plucking and removal of fur, hairs or whiskers). When the stressed partners received allogrooming, they did not display flinching behaviour that is indicative of agonistic interaction (Supplementary Video 1). Although allogrooming studied in the current paradigm probably represents an affiliative comforting behaviour, it remains a possibility that allogrooming may serve other behavioural and emotional functions (including affiliative, neutral or even agonistic) in other social contexts and could be related to the animals' behavioural and/or emotional states and social status.

Prosocial interaction following other types of stressors. Pairs of same-sex C57BL/6J mice that were co-housed for at least 5 weeks were used for examination of prosocial interaction in response to other types of stressors, including forced swim and acute restraint. The mice were habituated to human handling procedures and to the behaviour setup as described above. For evaluating prosocial interaction after the partner experiences forced swim, the partner was separated from the subject for 10 min and then placed into a beaker containing room-temperature (~20–22 °C) water. After 5 min, the partner was taken out and thoroughly dried with soft tissues as quickly as possible (within ~1–2 min) before being returned to the home cage. As a control, the same partner was separated from the subject for 14 min, placed in water and then taken out after ~5 s and thoroughly dried. Control experiments were performed one day before the stress experiment. For evaluating prosocial interactions after the partner experienced acute restraint, the partner was separated from the subject, kept in a restrainer for 30 min and then returned to the home cage. In the control experiments, the same partner was placed into a separate cage for 30 min before being returned to the home cage. Control experiments were performed one day before the stress experiments. Subject and partner behaviours were recorded, annotated and quantified as described above.

For assessing subject–partner interaction after partners experience chronic stress (Supplementary Note 2), one of the mice (the partner) in each same-sex, co-housed C57BL/6J pair was restrained in a restrainer for 3 h each day for ten consecutive days[29]. During these ten days, the subjects and partners were single-housed in separate cages, as subject–partner interactions may lead to a reduction of stress in the partners (Fig. 1u–w). On day 11, the partner did not receive any restraint and was placed into the cage containing the subject. In the control group, the mice were separated and single-housed for ten days without exposing the partners to restraint on each day.

Prosocial interaction after odour transfer. Pairs of same-sex C57BL/6J mice that were co-housed for at least 5 weeks were used for examining prosocial interaction in response to odours transferred from a naive or distressed donor mouse. Mice were habituated to human handling procedures and to the behaviour set-up for three consecutive days. Odours were transferred by wiping the anogenital area of a third donor mouse (group-housed) with a cotton swab and then wiping the anogenital area of the partner mouse. To habituate the partner and donor mice to the swab procedure, we performed this procedure on three consecutive days before the tests between the naive donor mouse and the partner mouse. For the unstressed donor test, the partner was removed from the home cage and an anogenital swab was performed between the naive donor and the partner. The partner was then reunited with the subject. For the stressed donor test, we subjected the donor to 20 foot shocks (0.7 mA, 1s) before performing the anogenital swab. Subject and partner behaviours were recorded, annotated and quantified as described above. The unstressed donor experiments were performed one day before the stressed donor experiments.

Evaluation of the stress-relieving effect of prosocial interaction. To examine the influence of naive subjects on the stress level of distressed partners, same-sex partners were separated from subjects and exposed to foot shocks as described above. Partners in the 'reunion' group were returned to their home cages and allowed to interact with subjects for 8 min. Partners in the 'alone' group were returned to their home cages in the absence of subjects and left undisturbed for 8 min. The partners were subsequently placed in the centre of an open field in a square chamber (50 × 50 × 50 cm) and allowed to freely explore the arena for 25 min. The locations of animals (defined as position of the centroid) were tracked using a custom program in MATLAB and were then used to calculate the time spent in the corners (four 12.5 × 12.5 cm areas). Baseline (no separation or foot shocks) data were collected one day

before the foot-shock procedures. Each partner in the reunion group was tested on the same day as a partner in the alone group in a matched manner to account for potential day-to-day variations in environmental factors that may affect the stress level. To assess the stress-reducing effect when naive subjects and stressed partners were prevented from close physical contact, a perforated barrier was placed in the middle of the cage with the naive subject and the stressed partner on each side during the reunion period. For the alone group, a perforated barrier was also placed in the middle of the cage with the stressed partner on one side. In Fig. 1u, v, to generate heat maps of the average occupancy time of partners at different locations in the open field, the open field was divided into 255 × 255 patches of equal area and the time that partners spent within each patch during a 25 min assay was averaged across all partners.

Microendoscopic calcium imaging

Behaviour assay. We used in vivo microendoscopic calcium imaging[30,31] of MeA neurons during free interaction with unstressed or stressed conspecifics. Subject mice were habituated to human handling procedures, the microendoscope and the behaviour set-up for at least three days before the experiments. During each imaging session, individual same-sex C57BL/6J mice (naive or stressed with 20 foot shocks at 0.7 mA, 1s, with a random interval between 10 s and 20 s) were placed into the home cage of the subject animals. The two animals were allowed to freely interact for 5–10 min. Each subject animal was presented with 2–6 unstressed and 2–6 stressed conspecifics during each imaging session. We performed seven independent imaging sessions in six subject animals. All subject animals were each imaged in one independent session, except for one animal that was imaged in two independent sessions at different focal planes. Calcium fluorescence videos and behaviour videos were simultaneously recorded using a microendoscope (UCLA Miniscope V4, purchased from Open Ephys; https://github.com/Aharoni-Lab/Miniscope-DAQ-QT-Software) and a video camera, respectively. The microendoscopes were connected to a digital acquisition device through a flexible, ultra-light coaxial cable. Behaviour videos were annotated by a human annotator frame by frame to identify the onset and offset times of behaviours exhibited by the subject animals.

Extraction of calcium signals. Calcium fluorescence videos were recorded at 30 Hz. Raw videos from each imaging session were processed using an integrated Miniscope Analysis package (https://github.com/etterguillaume/MiniscopeAnalysis). In brief, raw videos were first processed using the NormCorre algorithm (https://github.com/flatironinstitute/NoRMCorre)[32] for motion correction. Motion-corrected videos were then processed using Constrained Non-Negative Matrix Factorization (CNMF-E; https://github.com/zhoupc/CNMF_E)[33] to isolate cellular signals and associated regions of interest (ROIs). $\Delta F/F$ calcium traces of individual cells were z-scored and presented throughout in units of s.d. before downstream analysis. As CNMF-E can identify fluorescence changes from non-neuronal sources, such as motion artefacts or neuropil signals, we manually inspected extracted ROIs and traces to remove ROIs that lacked a soma-like shape and/or showed signs of motion artefacts in their traces. We obtained a total of 336 neurons from 7 independent imaging sessions in 6 subject animals.

Analysis of single-cell response during behaviour. A receiver operating characteristic (ROC) analysis[31,34] was used to identify neurons that significantly responded during each type of behaviour event. A binary threshold was applied to the $\Delta F/F$ signal to classify each time point as showing or not showing a particular behaviour. The true-positive rate and false-positive rate of behaviour detection were calculated over a range of binary thresholds spanning the minimum and maximum values of the neural signal and used to construct an ROC curve that describes how well the neural signal detects behaviour events at different thresholds. The area under the ROC curve (auROC) was then calculated as a measure of how strongly neural activity was modulated by each behaviour. The observed auROC was compared to a null distribution generated by circularly permuting the calcium signals by a random time shift 1,000 times. A neuron was considered significantly responsive ($\alpha < 0.05$) if its observed auROC value exceeded the 95th percentile of this null distribution (activated if auROC > 97.5th percentile or suppressed if auROC < 2.5th percentile). Note that suppressed cells that were defined using this method do not necessarily exhibit an immediate decrease of activity at the onset of behaviour, but display an overall negative correlation with the corresponding behaviour. In Fig. 2i, among all allogrooming-responsive neurons, 69.6% were activated and 30.4% were suppressed; among all sniffing-responsive cells, 63.0% were activated and 37.0% were suppressed. This ROC analysis was separately performed for each type of behaviour event and cells identified as responsive to more than one type of behaviour were defined as the mixed group in Fig. 2d, i.

To quantify average cell responses during different types of behaviour (Fig. 2e, f, k, l and Extended Data Fig. 3c, d, g), the activity of individual cells during each behaviour bout was aligned to the behaviour onset (time 0) and averaged across all of the behaviour bouts within each imaging session. The values of activity change were derived by subtracting the baseline activity, which was calculated as averaged activity over a 2 s time window between 5 s and 3 s before behaviour onset. Fig. 2f shows the average responses of cells activated by unstressed, but not stressed, conspecifics during sniffing of unstressed animals (blue curve) and of cells activated by stressed, but not unstressed, conspecifics during sniffing of stressed animals (orange curve). Fig. 2l shows the average responses of cells activated during allogrooming but not sniffing (left) and cells activated during sniffing but not allogrooming (right) during allogrooming (pink curves) and sniffing (green curves) events.

Analysis of population dynamics during behaviour. To analyse the relationship between population activity and behaviour, we first performed principal component analysis (PCA) on activity traces recorded from prosocial interaction sessions. Projection of population activity from individual sessions onto the top principal component yielded traces that appeared to be modulated during social interaction (Extended Data Fig. 4a). To examine the dynamics of dominant activity components during social interaction, we averaged PC1 projections around the onset of sniffing and allogrooming behaviour across all behaviour trials in all sessions. This trial-averaged response showed a clear time-locked increase in activity during social interaction (Extended Data Fig. 4b). Finally, to quantify the information contained in PC1 dynamics about social interaction, we examined how well this component alone could be used to decode behaviour. We constructed ROC curves to measure, in each session, the relationship between social interaction events and PC1 activity, and used the area under this curve (auROC) as a performance metric. We found that the auROC based on real data was significantly higher compared with that determined on the basis of circularly permuted behaviour vectors (control) (Extended Data Fig. 4c). These results suggest that the encoding of social interaction is saliently embedded in the dominant component of MeA neuronal dynamics.

To analyse the separation of population vectors associated with different types of behaviour (allogrooming, sniffing and self-grooming), we used PCA of trial-averaged neural responses during behaviour (within each independent session) to identify neural components that capture variability in the mean population response. To visualize the separation of population activity on these components, we projected activity during behaviour events onto the top two components (an example session is shown in Fig. 2o). We next sought to quantify the clustering of population activity patterns associated with individual behaviour events by event type. For each session, we computed the

average pairwise Euclidean distance between PC projections (on the top two PCs) of trial activity within a behaviour category, as well as the average pairwise distance between projections across behaviour categories. We compared these within-group distances with the between-group distances for each pair of behaviours. Larger between-group distances indicate that activity associated with behaviour events is clustered by event type, suggesting a separation of population activity patterns by behaviour type in PC space. PCA was performed using either manual behaviour annotations (Fig. 2o and Extended Data Fig. 4d) or deep-learning-based behaviour annotations (Extended Data Fig. 2g, h; see the 'Behaviour analysis using deep learning' section below) and revealed similar patterns of separation between population activities associated with different behaviours.

For behaviour decoder analyses, support vector machine (SVM) models were used to determine the hyperplanes that best separate population vectors associated with behaviour events versus baseline activity (single-behaviour decoders; Fig. 2m, n), or between distinct types of behaviour (between-behaviour decoders; Fig. 2h, p and Extended Data Fig. 4e, i).

For the binary between-behaviour decoders in Fig. 2h, p, decoder performance was computed independently for each session using a leave-one-out cross-validation procedure. For each session, the mean population activity associated with a behaviour event was considered to be a sample, and samples were taken for all instances of each of two behaviour types. For each validation fold, one sample was held out for testing, and the remaining samples were used for training. Any samples that fell within a time window (3 min in Fig. 2h; 1 min in Fig. 2p) of the test sample on a given fold were removed from the training set for that fold. Representation of training samples for each group was equalized on each fold by uniformly upsampling the group with fewer samples. For each fold, an SVM model was constructed using the training set and a prediction score was computed for the held-out sample. Finally, all prediction scores from all validation folds were compared with the ground truth sample labels using an ROC curve, and the area under this curve (auROC) was taken as the final performance metric. Chance performance was measured for each session by performing the same exact procedure, but first circularly permuting the activity trace for each neuron.

For decoder projections in Fig. 2m, single-behaviour decoders were constructed using samples of neural activity during behaviour and samples of baseline activity (5 s intervals during which sniffing, allogrooming and self-grooming were not observed). To obtain a projection over a continuous interval of test data, an entire session was split into two continuous 90% and 10% intervals. The samples contained in the 90% interval were used for SVM analysis to obtain the decoder hyperplane, and the held-out 10% data were then projected onto the component normal to this plane to obtain a continuous projection. Decoder predictions that exceeded the prediction threshold were coloured in example traces shown in Fig. 2m to be visually compared with the ground truth labels.

For behaviour decoder time courses (Fig. 2n and Extended Data Fig. 4i), single-behaviour (Fig. 2n) or between-behaviour (Extended Data Fig. 4i) SVM decoders were trained and tested using population activity at different time points relative to the true behaviour onset time. At each time point relative to behaviour onset (ranging from 30 s before to 30 s after behaviour at 1 s intervals), samples of population activity at that time point (averaged activity between 0.5 s before and 0.5 s after that time point) were taken (along with samples of baseline activity for Fig. 2n), and twentyfold cross validation was used to measure the decoder performance. To eliminate potential contamination of activity in the test samples by other neighbouring events, events of the same behaviour type that occurred within 2 min of any test data were removed from the training set for each fold. Representation of training samples for each group was equalized on each fold by uniformly upsampling the group with fewer samples. Time courses for shuffled decoders were computed using randomly circularly permuted activity traces. As the performance of these decoders was close to chance level before behaviour onset, did not peak until after behaviour onset and remained above chance level several seconds afterwards, it is unlikely that the distinct patterns of population activity associated with different behaviours were due to differences in behavioural events before behaviour onset (Extended Data Fig. 4f–h).

For the three-way multi-class decoder (Extended Data Fig. 4e), the procedure was similar to that for the binary between-behaviour decoders in Fig. 2h, p, except that samples from all three behaviour types (allogrooming, sniffing and self-grooming) were used in the training set. On each validation fold, one sample was held out, the remaining samples (outside of a 1 min window from the held-out sample) were equalized, a multi-class SVM model was constructed using the training data and behaviour identity (class label) was predicted for the held-out sample. The accuracy for each session (the overall fraction of correctly predicted group labels) was used as a performance metric and was compared with that of the decoders that were constructed using circularly permuted activity traces.

For prediction of short versus long allogrooming bouts using neural activity (Extended Data Fig. 4j, k), PC projections of neural activity within each session were pooled across sessions to construct one decoder. To pool samples of population activity across sessions, we transformed the population data into a common space of components that were shared across all sessions. To this end, we computed the trial-averaged dynamics for each neuron for each behaviour type (sniffing, allogrooming and self-grooming) and concatenated these across sessions. PCA of this cross-session neural activity matrix yielded components that capture the shared trial-averaged dynamics during similar behaviour events. The population activity within each session was then projected onto the top 12 shared components. For each allogrooming bout across all sessions, we extracted 24 measures of population activity around behaviour onset: projection onto the top 12 PCs averaged over the 3 s before behaviour onset, and projection onto those same components averaged over the 3 s after onset. Samples of these activity measures across allogrooming bouts from all sessions were concatenated, and SVM was used to find a hyperplane that separates short (≤5 s) versus long (>5 s) allogrooming bouts. Leave-one-out cross-validation and an ROC curve comparing predicted bout lengths with ground truth were used to measure the decoder performance (Extended Data Fig. 4j), and these were compared with control decoders using circularly permuted activity traces (Extended Data Fig. 4k). To increase the statistical power, this analysis also included baseline allogrooming bouts exhibited during interaction with unstressed animals, in addition to allogrooming behaviour towards stressed animals. All of the other analyses in Fig. 2i–p and Extended Data Figs. 3a–h, 4a–i specifically examined subject behaviours during prosocial interaction with stressed animals.

Behaviour analysis using deep learning

To characterize allogrooming behaviour in a more quantitative manner, we examined whether allogrooming contains unique and characteristic spatial and temporal features that can be reliably recognized using machine learning methods (Fig. 1o–r and Extended Data Fig. 2a–f). Previous machine learning analysis of behaviour was based primarily on body and pose tracking[35–39], but as both allogrooming and conspecific sniffing involve close-range interactions that lead to occlusion between animals, individual body parts are not reliably trackable (especially when animals have the same coat colour), rendering the analysis of fine behavioural features difficult. To extensively capture spatial features that are relevant to behaviour, we implemented a deep CNN model (Google Inception v3)[40,41] that was pretrained on a large image dataset consisting of 1.2 million images (ImageNet). We implemented the Google Inception v3 model in Python (v.3.5.6) using the TensorFlow package (v.1.11). Using this network, we extracted 2,048 spatial features

from each frame in an unsupervised manner (without training the CNN on the current dataset). Behaviour videos that were recorded during the microendoscopic imaging experiments were used for this analysis, as this enabled us to collect head-orientation information through a high-precision gyroscope attached to the microendoscope and to compare the model performance using different behavioural features (see below). Videos were recoded using a 2.0 megapixel USB camera (ELP) at 30 f.p.s. with a 640 × 320 pixel image size from a side view. The videos were annotated by an experienced human annotator to identify each frame as one of the four behaviour classes—allogrooming, sniffing, self-grooming or other behaviour, and this was used as the ground truth for model training and evaluation.

To further evaluate whether the CNN comprehensively captures behaviourally relevant features, we sought to extract additional tracking-based features such as location and pose as well as head orientations. To extract spatial features on the basis of animal and pose tracking, we used SLEAP[42]. As the animals are of the same colour and because allogrooming and sniffing involve close-range interactions between the animals that lead to substantial occlusion, reliable tracking of fine body parts (such as heads, ears, snouts and paws) was not feasible. Instead, we tracked the body locations of the subject animals and the partners as well as the position of the head-mounted microendoscope as a proxy of the head location of the subject animals. From these values, we further calculated the distance between the subject's head and the partner's body, the distance between the bodies of the two animals, and the speeds of both animals. To acquire head orientation and rotation features that capture fine head movement in three-dimensional space, we used a high-precision three-axial gyroscope (BNO055, Bosch Sensortec) attached to the microendoscope on the subject animals during microendoscopic imaging. Raw quaternions measuring three-axial orientations were recorded with a high temporal precision (30 Hz). Quaternions were then converted to Euler angles at each time point. From these values, we further calculated the changes in Euler angles of each of the three axes and the angular velocity of the dorsal–ventral axis of the head at each time point.

To extract temporal features in sequences of frames and to classify behaviours on the basis of their spatiotemporal patterns, we constructed a long short-term memory (LSTM)-based RNN model[43,44] in Python using the TFLearn module in TensorFlow. We passed CNN-derived features, tracking-based features, head orientation-based features or all of the above to the RNN model. Our model comprises an input layer, a LSTM layer with 256 nodes, followed by a fully connected softmax layer and a final regression layer. We also explored other RNN structures, including one LSTM layer with 128 or 512 nodes and two LSTM layers with 128 nodes each, and found that the current structure achieved the highest performance. To generate temporal sequences for RNN training and testing, we downsampled the videos to 15 f.p.s. and used a custom Python script to generate 30-frame (2 s) sequences with a shift of seven or more frames between adjacent sequences. We divided the whole dataset into training, validation and test sets (80%, 10% and 10% of the data, respectively) and assigned sequences generated from different segments of the videos as training and test sets such that there was minimal temporal overlap between the two sets. To generate shuffled data as a control, we randomly permuted the behaviour labels of the sequences. During training, the Adam optimization algorithm was used for gradient descent. The prediction accuracy on the validation set was evaluated during training to prevent over-fitting. Models using CNN-derived features or all three types of features were trained for 75 epochs, at which point validation accuracy plateaued. Models using tracking-based or head-orientation-based features reached optimum performance after 20 and 10 epochs, respectively; further training led to a decrease in the validation and test performance, indicating over-fitting.

We trained binary classifiers to discriminate between pairs of behaviour classes (Fig. 1p and Extended Data Fig. 2b–e) and multi-way classifiers to discriminate between all four behaviour classes (Extended Data Fig. 2f). To evaluate the performance of the models, we calculated the F_1 score as follows, which takes into account both the precision and recall of prediction:

$$F_1 = 2 \times \frac{\text{precison} \times \text{recall}}{\text{precison} + \text{recall}}$$

We performed tenfold cross-validation and compared the distribution of F_1 scores between different models. For the four-way classifier, we calculated averaged F_1 scores across all four classes. We found that using tracking- or head-orientation-based features alone led to a lower classification performance compared with using CNN-derived features, and combining CNN-derived features with tracking and head orientation achieved a performance similar to that of CNN features alone (Extended Data Fig. 2f). This suggests that unsupervised features extracted from the CNN contain rich information that is not further augmented by tracking and head orientation features.

To perform *t*-SNE embedding of spatiotemporal features of different behaviour types (Fig. 1r), we first performed PCA using the fast.prcomp function in the gmodels R package. PCs 1–30 were then used as input for *t*-SNE to generate a two-dimensional nonlinear embedding using the Rtsne function in the Rtsne R package, with 1,000 iterations and a perplexity parameter of 30.

Optogenetics experiments

After stereotaxic surgeries, the viruses were allowed to incubate for 4–7 weeks before behavioural testing. Before an experiment, a ferrule patch cord was coupled to the ferrule fibre implanted in the subject mouse using a zirconia split sleeve (Doric Lenses). Optical fibres were connected using an FC/PC adaptor (Doric Lenses) to a 473 nm blue laser (CNI Laser). An Arduino microcontroller board and a customized MATLAB program were used to control laser pulses. The partner was separated from the subject and exposed to foot shocks as described above before being reunited with the subject.

In the *Gt*ACR2 inhibition experiments, blue (473 nm) light was delivered continuously for 5 s at an irradiance of ~8–10 mW mm^{-2} in the target region when the subject exhibited spontaneous allogrooming towards the stressed partner. Real and sham light illumination was manually triggered alternately but no light was delivered during the sham trials. Male subjects were used for the inhibition experiments, as they provided a relatively high level of allogrooming towards stressed partners for assessing the suppressing effect of light illumination.

Initial optogenetic screening of MeA neuronal subpopulations (Fig. 3k–m and Extended Data Fig. 5a–p) using different Cre driver lines (*Tac1*$^{cre/+}$, *Sst*$^{cre/+}$ and *Cck*$^{cre/+}$) was performed using 15–20 ms, 473 nm pulses at 15–20 Hz for 15 s, at an irradiance of around 6–10 mW mm^{-2} in the target region. In this initial screening, a same-sex BALB/cJ mouse was used as a target animal. *Tac1*$^+$, *Sst*$^+$ and *Cck*$^+$ neurons constitute 18.4%, 16.1% and 9.1% of MeA GABAergic neurons, respectively, on the basis of single-cell RNA-sequencing data (Gene Expression Omnibus: GSE124061)[18,45]. These Cre lines were generated by knocking *cre* into the endogenous loci of the corresponding genes and were previously validated to recapitulate their endogenous expression patterns[46–48].

The effect of soma stimulation in *Vgat*$^{flp/+}$; *Tac1*$^{cre/+}$ mice injected with Con/Fon-ChR2 or Coff/Fon-ChR2 was assessed in the presence of stressed partners (Fig. 4e (left), 4f and Extended Data Figs. 6a–g and 10d–f) or unstressed partners (Fig. 4e (right)) using 473 nm, 7–15 ms pulses at 7–15 Hz for 15 s, at an irradiance of around 4–6.5 mW mm^{-2} in the target region. Under the same stimulation conditions, the activation of Tac1$^+$Vgat$^+$ neurons elicited allogrooming but not attack behaviour towards stressed partners (Fig. 4e, g) whereas activation of Tac1$^-$Vgat$^+$ neurons elicited a substantial level of attack but minimal allogrooming (Extended Data Fig. 10d–f and Supplementary Note 6).

Soma stimulation in *Vgat*$^{flp/+}$; *Tac1*$^{cre/+}$ mice injected with Con/Foff-ChR2 (Extended Data Fig. 7d–f) was performed using 20 ms, 473 nm pulses at 20 Hz for 15 s, at an irradiance of ~12 mW mm^{-2} in the target region. The effect of stimulation was assessed both in the presence and absence of stressed partners (data presented in Extended Data Fig. 7d–f were from experiments with stressed partners). We observed a robust induction of self-grooming in both contexts and did not observe any notable difference in the behaviour induced between the two contexts.

We observed axonal projections of MeA$^{Tac1\cap Vgat}$ neurons in the MPOA and PMv (Extended Data Fig. 8a, b, p), consistent with previous characterizations of projection targets of MeA neurons in general[23,49]. Stimulation of MPOA projection in *Vgat*$^{flp/+}$; *Tac1*$^{cre/+}$ animals (Fig. 4p–s) was performed using 10 ms, 473 nm pulses at 20–40 Hz for 10 s, at an irradiance of ~8 mW mm^{-2} in the target region. Stimulation of PMv projection in *Vgat*$^{flp/+}$; *Tac1*$^{cre/+}$ animals (Extended Data Fig. 8q) was performed using 10 ms, 473 nm pulses at 50–60 Hz for 10 s, at an irradiance of around 10–15 mW mm^{-2} in the target region. Soma stimulation through retrograde targeting in *Vgat*$^{flp/+}$; *Tac1*$^{cre/+}$ mice (Fig. 4l–o) was performed using 20 ms, 473 nm pulses at 20 Hz for 15 s, at an irradiance of ~9–12 mW mm^{-2} in the target region. This stimulation did not promote any attack behaviour, even at these relatively high stimulation settings. Moreover, partners did not show obvious flinching behaviour when they received allogrooming from subject animals, consistent with an affiliative nature of the stimulation-evoked allogrooming.

For activation of the MeA-to-MPOA projection with inhibition of MeA cell bodies using lidocaine[50] (Extended Data Fig. 8m–o), stylets were removed from the guide cannulas before behavioural assays and 10 μg lidocaine (20 mg ml^{-1} in saline, injection volume 500 nl) was injected with a 26-gauge needle into the MeA immediately before the behaviour assay. Injection needles remained in place for an additional 2 min before being removed and replaced immediately with stylets.

In the ChR2-activation experiments in *Vgat*$^{cre/+}$ animals, we found that a high stimulation intensity (20 ms, 473 nm pulses at 20 Hz for 15 s, at an irradiance of ~9 mW mm^{-2} in the target region) elicited attack behaviour, as has been previously reported[17] (data not shown). At lower stimulation intensity (7–15 ms, 473 nm pulses at 7–15 Hz for 15 s, at an irradiance of ~4–6.5 mW mm^{-2} in the target region), light stimulation was able to trigger allogrooming without inducing attack behaviour towards stressed partners in 5/6 male mice and 7/9 female mice (Extended Data Fig. 9b). To examine the effect of low-intensity photostimulation of Vgat^{+} neurons during interaction with unfamiliar intruders, we introduced an unfamiliar C57BL/6J male intruder into the home cage of the subject animal. The behavioural effects of photostimulation during interaction with stressed partners or unfamiliar intruders were compared in the same subject animals with the same stimulation parameters (Supplementary Note 6).

In ChR2-activation experiments, we found that the duration of triggered allogrooming was higher when subject animals were in the vicinity of and attending to the partners compared with that across all stimulations (Extended Data Fig. 9d). Thus, quantifications presented in all of the other figures were based on laser stimulations that were delivered when subject animals were in the vicinity of (within half a body-length) and attending to the partners or intruders. Light stimulations were delivered during periods at which subject animals did not exhibit high levels of spontaneous allogrooming or other behaviours of interest.

Behaviours and stimulation bouts in optogenetic experiments were annotated in a frame-by-frame manner by an experienced human annotator. To calculate the probability of showing a particular behaviour at different time points relative to the onset of light illumination (Figs. 3l and 4e, f, m, q and Extended Data Figs. 5a–f, i–n, 6a, d, 7d, e, 8m, n and 10d, e), trials from all animals were aligned to the onset of light illumination and the fraction of trials showing a particular behaviour at a given time point (30 time points per second) was calculated as the probability of showing that behaviour. The duration of behaviour was calculated as the total amount of time that animals spent on a particular behaviour during the period of light illumination or sham manipulation (Figs. 3d, m, n and 4g, n, r and Extended Data Figs. 5g, h, o, p, 6b, e, g, 7f, 8d, f, i, k, o, q, 9b–d and 10f). For trials during which allogrooming did not occur, onset latency was calculated as the length of the stimulation (Fig. 4o, s and Extended Data Figs. 6c, f and 8e, g, j, l).

Fibre photometry

After stereotaxic surgeries, the viruses were allowed to incubate for around 4 weeks before recording experiments. Fluorescence signals were acquired with a fibre photometry system (Doric Lenses). The analogue voltage signals were digitalized and recorded by a Micro1401 digitizer (CED) using Spike2 (v.10.09a). The LED power was adjusted at the tip of the optical fibre to around 5–10 μW. A ferrule patch cord was connected to the ferrule fibre implanted in the subject mouse using a zirconia split sleeve (Doric Lenses). The partner was separated from the subject and exposed to foot-shocks as described above. Recording was started immediately before the stressed partner was reunited with the subject. Photometry data were exported to MATLAB files for further analysis. Behaviour was recorded, annotated frame-by-frame and aligned to calcium signals. The values of fluorescence change ($\Delta F/F$) were derived by calculating $(F - F_0)/F_0$, where F_0 is the baseline fluorescence signal averaged over a 0.5 s time window between 1 s and 0.5 s before each behaviour bout. $\Delta F/F$ values are presented as mean ± s.e.m. (shading) (Figs. 3g and 4j and Extended Data Fig. 5q). Consecutive allogrooming bouts with an interval of <1 s between them were considered to be one continuous bout. Allogrooming bouts that lasted for at least 2 s were used for analysis. We also calculated mean $\Delta F/F$ values during the entire allogrooming bout (if bout duration ≤5 s) or the first 5 s after behaviour onset (if bout duration >5 s) (Figs. 3h and 4k and Extended Data Fig. 5r). The aforementioned methods were applied for both the GCaMP and eYFP groups. To assess whether there may be a habituation of MeA neural activity during allogrooming over the course of a recording session, we divided allogrooming bouts within each recording session in MeA^{Vgat} neurons into three groups on the basis of their temporal order (the first, second and last thirds of all bouts). We found no significant difference in mean AUC between these three groups (n = 6–16 allogrooming bouts in each group; mean ± s.e.m., 5.7 ± 1.6%, 5.3 ± 2.8% and 8.5 ± 3.8%; Kruskal–Wallis test, P = 0.7239), suggesting that there was no overall decay in MeA^{Vgat} neuron activation during allogrooming over time.

Histology

Animals were euthanized and perfused with 4% paraformaldehyde (PFA). The brains were dissected out and fixed in 4% PFA for 2 h at room temperature, rinsed with 1× PBS, then placed in 30% sucrose overnight at 4 °C. Sections (60 μm) were cut using a Leica CM1950 cryostat. Images were acquired using a Leica DM6 B microscope or a confocal microscope (Zeiss LSM 880).

Fluorescence mRNA in situ hybridization and immunohistology

To examine the expression of different genes in different MeA neuronal subpopulations (Figs. 3i, j and 4b, c and Extended Data Figs. 7c, 10c), we performed mRNA in situ hybridization and immunohistology. In situ hybridization was performed on fixed brain tissues using the RNAscope technology (ACDbio, 323110). Mice were perfused with PBS and 4% PFA. Brains were post-fixed in 4% PFA for 8 h at 4 °C and then dehydrated in 20% sucrose overnight. Sections (14 μm) were obtained using a cryostat and kept at −80 °C before use. The staining procedures were performed according to the manufacturer's protocols for fixed-frozen tissue samples with some modifications. For co-staining of Tac1, Cck and Sst, the tissue was digested with protease III for 15 min at 40 °C. For the combination of RNAscope with

immunostaining, the tissue was target-retrieved for 5 min using the co-detection target retrieval buffer and treated with protease plus for 11 min at 40 °C to reduce overdigestion of antigen in eYFP. Immunostaining of eYFP was performed after the RNAscope procedures, but before 4,6-diamidino-2-phenylindole (DAPI) staining. In brief, the tissue was incubated with rabbit anti-GFP antibodies (Invitrogen, A-11122) diluted at 1:500 in a co-detection solution (ACDbio, 323180) at 4 °C overnight after RNAscope staining and then washed with PBST three times and incubated with donkey anti-rabbit-IgG secondary antibodies (1:500 dilution, Invitrogen, A-21206) for 2 h at room temperature. Finally, sections were stained with DAPI for 40 s and mounted with 70% glycerol. Images were acquired using Zeiss LSM 880 at 20× and analysed using QuPath[51] according to instructions from ACDbio. In brief, for the co-staining of Tac1, Cck and Sst, the DAPI channel was used to segment cell nuclei. A cell was classified as positive for a particular mRNA transcript if it contained >4 fluorescent puncta for the corresponding probe. In Fig. 3j, the fraction of overlap between a particular pair of markers was defined as the fraction of double-positive cells within all cells that were positive for either of the two markers. Owing to strong eYFP signals in the neurites, cell bodies with eYFP signals were manually identified and marked in QuPath. A cell was considered to be positive for Tac1, Vgat or Vglut2 if it contained >4 fluorescent puncta for the corresponding probe (Fig. 4b, c and Extended Data Figs. 7c and 10c). The probes used in this study include Tac1 (Mm-Tac1-T3), Cck (Mm-Cck-C3), Sst (Mm-Sst-C4), Vgat (Mm-Slc32a1-C2) and Vglut2 (Mm-Slc17a6-C2).

Owing to the design strategy of the Con/Fon-ChR2-eYFP viral construct[26], intermediate mRNA molecules are transcribed from the viral construct before Cre- or Flp-mediated recombination. Although these intermediate mRNA molecules do not express functional ChR2 and eYFP proteins, they contain part of the sequences that are recognizable by the same hybridization probes for the functional *ChR2* or *eYFP* mRNAs. As a consequence, immunohistology for the functional protein product was required for detecting the proper expression of the full-length, functional mRNA transcript after Cre- or Flp-mediated recombination. Moreover, as ChR2 proteins are primarily localized to membranes, their expression in cell bodies is difficult to visualize. We therefore used the corresponding Con/Fon-eYFP viral construct to perform simultaneous in situ hybridization for *Tac1* and *Vgat* mRNAs and immunohistology for eYFP proteins (Fig. 4b, c). For the same reasons, we used Con/Foff-eYFP (Extended Data Fig. 7c) or Coff/Fon-eYFP (Extended Data Fig. 10c) viral constructs to examine the co-localization of eYFP with Tac1, Vgat or Vglut2 in $Tac1^{cre/+}/Vgat^{flp/+}$ animals. Mice were perfused for in situ hybridization and/or immunohistology ~2–3 weeks after virus injection. The Cre-on/Flp-off virus used in the current study has been reported to result in residual expression in a minor fraction of $Cre^{+}Flp^{+}$ cells, possibly due to insufficiency of Flp relative to Cre[26,52]. We found that, when using this virus, although a fraction of $eYFP^{+}$ cells were $Vglut2^{-}$, the majority (mean ± s.e.m., 64.0 ± 1.8%) were glutamatergic ($Vglut2^{+}$).

Statistics and reproducibility

All statistical analyses were conducted using Prism (v.9, GraphPad), MATLAB (R2018a and R2019b, MathWorks), R (v.3.4.3) or Python (v.3.5.6). Statistical tests used in this study include Wilcoxon rank-sum tests, Wilcoxon signed-rank tests, *t*-tests, Kolmogorov–Smirnov tests, Kruskal–Wallis tests, Friedman tests, one-way analysis of variance (ANOVA) and two-way repeated-measures ANOVA. When parametric tests were used, data normality and homogeneity of variances were confirmed using the Shapiro–Walk normality test and Levene's test, respectively. *P* values were corrected for multiple comparisons when necessary. The bar plots show the mean ± s.e.m. In the box plots, the centre lines indicate the median, the box limits indicate the upper and lower quartiles, the whiskers indicate data within 1.5× the interquartile range, and the dots indicate data points outside the 1.5× interquartile range (except in Extended Data Fig. 4k, in which the whiskers indicate the 2.5th and 97.5th percentiles and the dots indicate data points outside this range). The significance threshold was held at $\alpha = 0.05$; NS, not significant ($P > 0.05$); $^{*}P < 0.05$, $^{**}P < 0.01$, $^{***}P < 0.001$. More detailed information for all statistical analyses (including the sample sizes, types of statistical test, test statistics and exact *P* values when $P > 0.0001$) that are presented in the figures and extended data figures is provided in Supplementary Table 1. All behavioural, imaging and optogenetics experiments were replicated in multiple subject animals with similar results (the exact *n* numbers of animals and/or trials for each experiment are provided in Supplementary Table 1 and the figure legends). Example micrographs (Figs. 2b, 3b, i and 4a, b and Extended Data Figs. 3i, 7c, 8a, b, p and 10c) show representative results based on at least three independent biological samples (animals or independently injected brain hemispheres). Sample sizes were not predetermined using statistical methods. Experiments were randomized whenever possible. Experimenters were not blind to group allocation.

Reporting summary

Further information on research design is available in the Nature Research Reporting Summary linked to this paper.

Data availability

Additional data relating to the paper are available from the corresponding author on reasonable request. Source data are provided with this paper.

Code availability

Code for the behavioural analysis (https://github.com/pdollar/toolbox), animal pose tracking (https://github.com/murthylab/sleap/releases/tag/v1.0.9), microendoscopic imaging data analysis (https://github.com/etterguillaume/MiniscopeAnalysis, https://github.com/zhoupc/CNMF_E and https://github.com/flatironinstitute/NoRMCorre) is available at GitHub. The pretrained Google Inception v3 network is available online (https://download.tensorflow.org/models/image/imagenet/inception-2015-12-05.tgz). Additional code relating to the paper is available from the corresponding author on reasonable request.

23. Canteras, N. S., Simerly, R. B. & Swanson, L. W. Organization of projections from the medial nucleus of the amygdala: a PHAL study in the rat. *J. Comp. Neurol.* **360**, 213–245 (1995).
24. Cádiz-Moretti, B., Otero-García, M., Martínez-García, F. & Lanuza, E. Afferent projections to the different medial amygdala subdivisions: a retrograde tracing study in the mouse. *Brain Struct. Funct.* **221**, 1033–1065 (2016).
25. Mahn, M. et al. High-efficiency optogenetic silencing with soma-targeted anion-conducting channelrhodopsins. *Nat. Commun.* **9**, 4125 (2018).
26. Fenno, L. E. et al. Targeting cells with single vectors using multiple-feature Boolean logic. *Nat. Methods* **11**, 763–772 (2014).
27. Chen, T.-W. et al. Ultrasensitive fluorescent proteins for imaging neuronal activity. *Nature* **499**, 295–300 (2013).
28. Dana, H. et al. High-performance calcium sensors for imaging activity in neuronal populations and microcompartments. *Nat. Methods* **16**, 649–657 (2019).
29. Lim, B. K., Huang, K. W., Grueter, B. A., Rothwell, P. E. & Malenka, R. C. Anhedonia requires MC4R-mediated synaptic adaptations in nucleus accumbens. *Nature* **487**, 183–189 (2012).
30. Ghosh, K. K. et al. Miniaturized integration of a fluorescence microscope. *Nat. Methods* **8**, 871–878 (2011).
31. Kingsbury, L. et al. Correlated neural activity and encoding of behavior across brains of socially interacting animals. *Cell* **178**, 429–446 (2019).
32. Pnevmatikakis, E. A. & Giovannucci, A. NoRMCorre: an online algorithm for piecewise rigid motion correction of calcium imaging data. *J. Neurosci. Methods* **291**, 83–94 (2017).
33. Zhou, P. et al. Efficient and accurate extraction of in vivo calcium signals from microendoscopic video data. *Elife* **7**, e28728 (2018).
34. Kingsbury, L. et al. Cortical representations of conspecific sex shape social behavior. *Neuron* **107**, 941–953 (2020).
35. Hong, W. et al. Automated measurement of mouse social behaviors using depth sensing, video tracking, and machine learning. *Proc. Natl Acad. Sci. USA* **112**, E5351–E5360 (2015).
36. Wiltschko, A. B. et al. Mapping sub-second structure in mouse behavior. *Neuron* **88**, 1121–1135 (2015).

37. Kabra, M., Robie, A. A., Rivera-Alba, M., Branson, S. & Branson, K. JAABA: interactive machine learning for automatic annotation of animal behavior. *Nat. Methods* **10**, 64–67 (2013).
38. Jhuang, H. et al. Automated home-cage behavioural phenotyping of mice. *Nat. Commun.* **1**, 68 (2010).
39. Nilsson, S. R. et al. Simple Behavioral Analysis (SimBA)—an open source toolkit for computer classification of complex social behaviors in experimental animals. Preprint at *bioRxiv* https://doi.org/10.1101/2020.04.19.049452 (2020).
40. LeCun, Y., Bengio, Y. & Hinton, G. Deep learning. *Nature* **521**, 436–444 (2015).
41. Szegedy, C., Vanhoucke, V., Ioffe, S., Shlens, J. & Wojna, Z. Rethinking the inception architecture for computer vision. Preprint at https://arxiv.org/abs/1512.00567v3 (2015).
42. Pereira, T. D. et al. SLEAP: multi-animal pose tracking. Preprint at *bioRxiv* https://doi.org/10.1101/2020.08.31.276246 (2020).
43. Hochreiter, S. & Schmidhuber, J. Long short-term memory. *Neural Comput.* **9**, 1735–1780 (1997).
44. Lipton, Z. C., Berkowitz, J. & Elkan, C. A critical review of recurrent neural networks for sequence learning. Preprint at https://arxiv.org/abs/1506.00019 (2015).
45. Wu, Y. E., Pan, L., Zuo, Y., Li, X. & Hong, W. Detecting activated cell populations using single-cell RNA-seq. *Neuron* **96**, 313–329 (2017).
46. Harris, J. A. et al. Anatomical characterization of Cre driver mice for neural circuit mapping and manipulation. *Front. Neural Circuits* **8**, 76 (2014).
47. Taniguchi, H. et al. A resource of Cre driver lines for genetic targeting of GABAergic neurons in cerebral cortex. *Neuron* **71**, 995–1013 (2011).
48. Daigle, T. L. et al. A suite of transgenic driver and reporter mouse lines with enhanced brain-cell-type targeting and functionality. *Cell* **174**, 465–480 (2018).
49. Hu, R. K. et al. An amygdala-to-hypothalamus circuit for social reward. *Nat. Neurosci.* **24**, 831–842 (2021).
50. Stuber, G. D. et al. Excitatory transmission from the amygdala to nucleus accumbens facilitates reward seeking. *Nature* **475**, 377–380 (2011).
51. Bankhead, P. et al. QuPath: open source software for digital pathology image analysis. *Sci. Rep.* **7**, 16878 (2017).
52. Fenno, L. E. et al. Comprehensive dual- and triple-feature intersectional single-vector delivery of diverse functional payloads to cells of behaving mammals. *Neuron* **107**, 836–853 (2020).

Acknowledgements We thank V. Wan and P. B. Chen for technical assistance and contributions to the project; D. Aharoni, P. Golshani and P. Zhao for assistance in setting up the miniscope (v4) imaging system; D. J. Anderson for comments and feedback on the project; and members of the Hong laboratory for valuable comments. Illustrations of mice and mouse brain schematics in Figs. 1a, u–x, 2a, 3a, e, k and 4d, h, l, p and Extended Data Figs. 7b, 8c, h, 9a and 10b were created using BioRender.com. This work was supported in part by NIH grants (R01 NS113124 and U01 NS122124), a Searle Scholars Award, a Packard Fellowship in Science and Engineering, a Keck Foundation Junior Faculty Award, a McKnight Scholar Award, a Vallee Scholar Award, a Mallinckrodt Scholar Award, a NARSAD Young Investigator grant, a Klingenstein-Simons Fellowship Award and a Brain Research Foundation grant (to W.H.) and NIH training grant (T32 NS048004, to J.D.).

Author contributions Y.E.W. and W.H. designed the study. Y.E.W., J.D., M.Z., F.S. and R.K.H. performed experiments. Y.E.W., W.H., L.K., J.D., M.Z. and F.S. analysed data. Y.E.W. and W.H. wrote the manuscript with inputs from J.D. and L.K. W.H. supervised the entire study.

Competing interests The authors declare no competing interests.

Additional information

Supplementary information The online version contains supplementary material available at https://doi.org/10.1038/s41586-021-03962-w.

Correspondence and requests for materials should be addressed to Ye Emily Wu or Weizhe Hong.

Peer review information *Nature* thanks Steve Chang and the other, anonymous, reviewer(s) for their contribution to the peer review of this work.

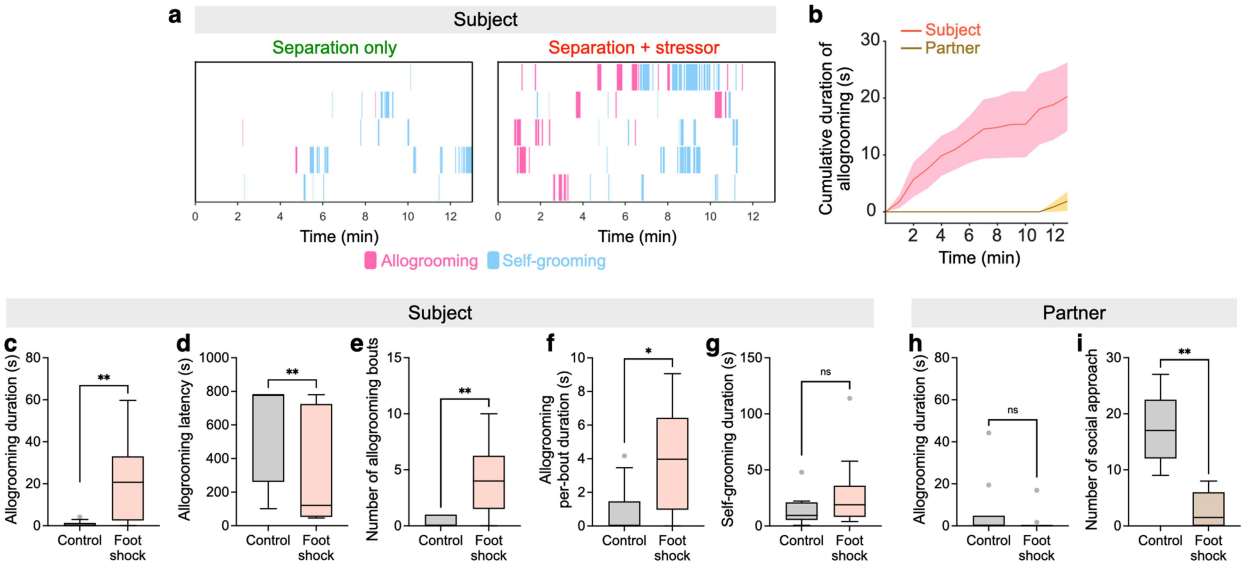

Extended Data Fig. 1 | Characterization of prosocial allogrooming in female mice. a, Example raster plots showing allogrooming and self-grooming behaviours exhibited by female subjects when they interact with unstressed (separation only, control) or stressed (foot-shocked) female partners. Each row represents an individual animal. **b**, Time-course of cumulative duration of allogrooming exhibited by subjects and partners after partners experience foot-shocks. Mean ± s.e.m. **c**, **d**, Total duration (**c**) and onset latency (**d**) of allogrooming exhibited by subjects toward unstressed (control) or foot-shocked partners during 13 min of interaction. While females exhibit elevated allogrooming toward stressed partners similar to males, the total duration of allogrooming toward stressed partners is shorter in females compared to males (Fig. 1d, Supplementary Note 1). **e**, **f**, Total number of allogrooming bouts (**e**) and average per-bout duration of allogrooming (**f**) in individual subjects interacting with unstressed (control) or foot-shocked partners. **g**, Total duration of self-grooming exhibited by subjects during interaction with unstressed (control) or foot-shocked partners. **h**, **i**, Total duration of allogrooming (**h**) and total number of social approaches (**i**) toward subjects exhibited by partners after separation only or foot-shocks. Boxplots: median with quartiles, 1.5 × IQR and outliers. **b**-**i**, $n = 10$ pairs of female mice. Two-sided Wilcoxon signed-rank test. $^{**}P < 0.01$, $^{*}P < 0.05$. ns, not significant. For details of statistical analyses, see Supplementary Table 1.

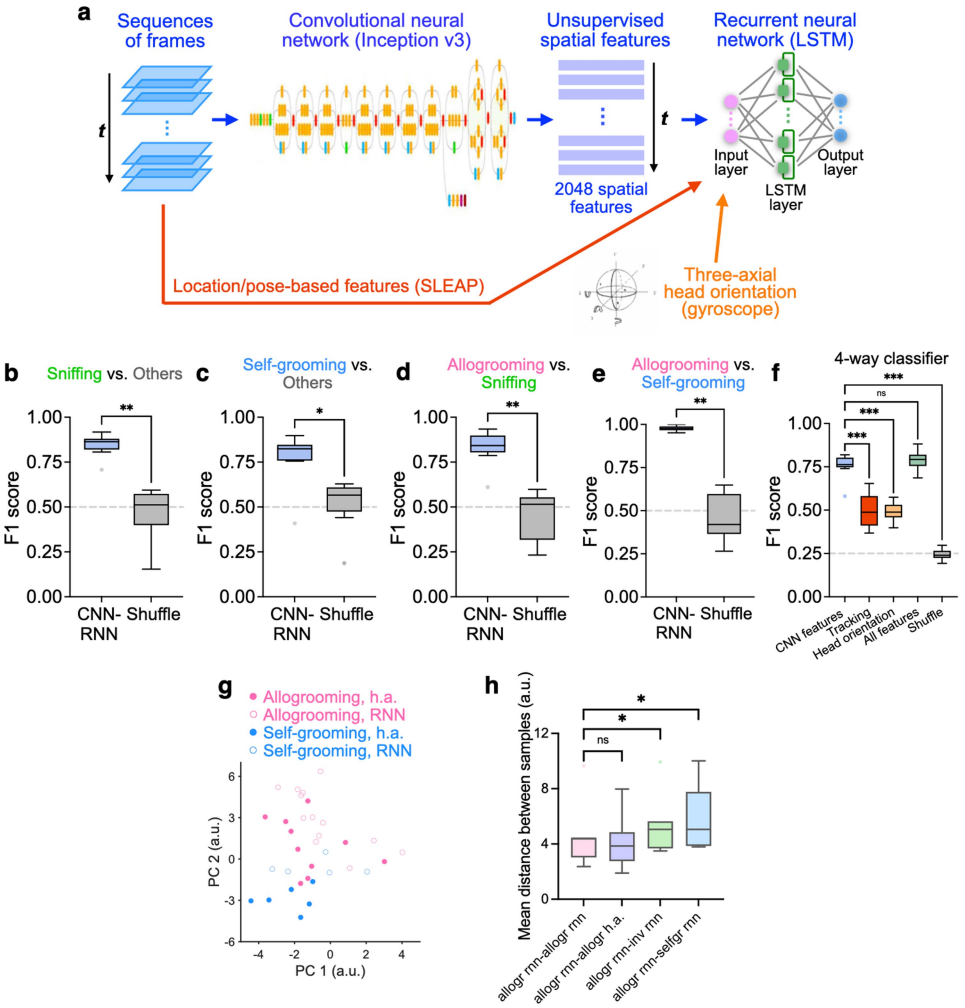

Extended Data Fig. 2 | Behavioral analysis using convolutional and recurrent neural networks. a, Schematic of behavior classification using recurrent neural network (RNN) based on CNN-derived spatial features, tracking-based features, and/or head orientation-based features. **b**–**e**, Performance of binary classifiers trained to discriminate between different pairs of behaviors using the CNN + RNN framework. **f**, Comparison of performance of four-way multi-class classifiers trained to discriminate between allogrooming, sniffing, self-grooming, or other behaviors. Different classifiers used CNN-derived spatial features, tracking-based features, head orientation-based features, or all three types of features to train the recurrent neural network. Data for the "CNN features" and shuffled control groups are the same as those in Fig. 1q and are presented here for comparison. **g**, PC projections of population vectors associated with different types of behavior bouts from one example microendoscopic imaging session. PCA is first performed using population activity during manually annotated behavior bouts (dots). Population activity during behavior bouts predicted using the CNN-RNN method (circles) was then projected onto this PC space. **h**, Mean pairwise Euclidean distances (in a space defined by PCs 1-4) between different pairs of behavior events that were either human annotated ("h.a.") or predicted using the CNN-RNN method during each independent imaging session. Boxplots: median with quartiles, 1.5 × IQR and outliers. **b**–**f**, $n = 9$ different partitions of training/validation/test datasets in each group. **h**, $n = 7$ independent imaging sessions in 6 subject mice. **b**–**e**, Two-sided Wilcoxon signed-rank test. **f**, One-way ANOVA followed by Bonferroni's multiple comparisons test. **h**, Friedman test followed by post hoc Dunn's multiple comparisons test. ***$P < 0.001$, **$P < 0.01$, *$P < 0.05$. ns, not significant. For details of statistical analyses, see Supplementary Table 1.

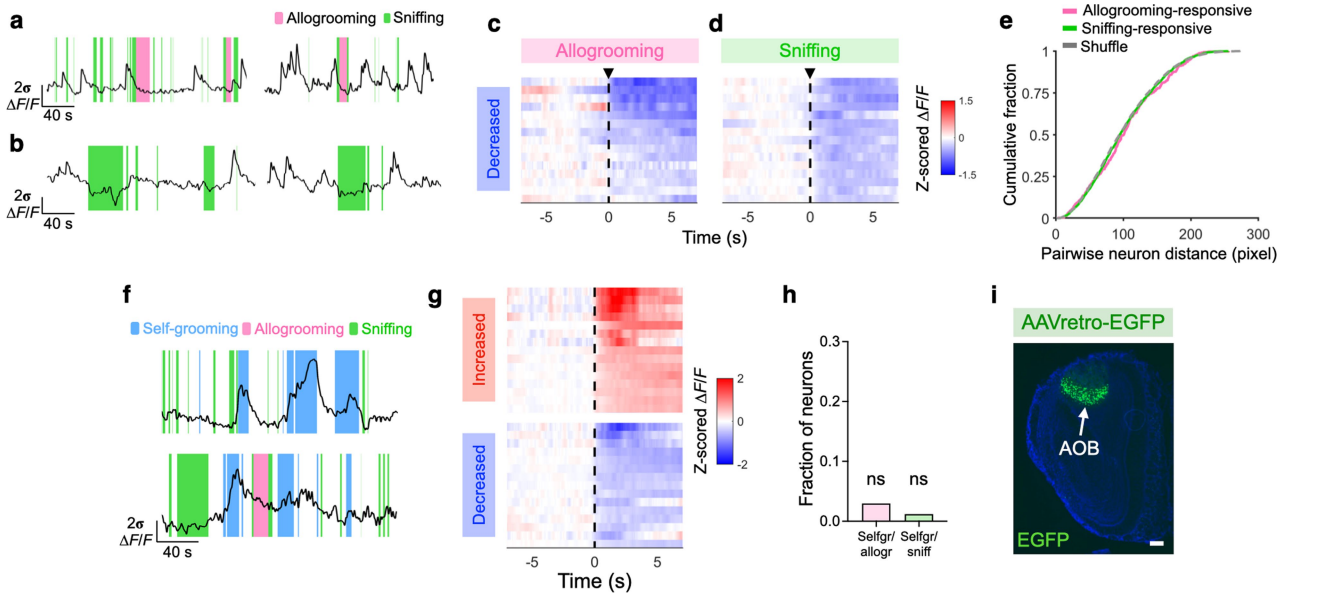

Extended Data Fig. 3 | MeA neuronal responses during prosocial interaction. a, **b**, Example calcium traces from individual allogrooming-suppressed (**a**) and sniffing-suppressed (**b**) neurons during allogrooming or sniffing toward stressed conspecifics. **c**, **d**, Heatmaps showing average responses of example neurons with decreased activity during allogrooming (**c**) or sniffing (**d**). **e**, Cumulative distributions of pairwise distances between neurons of the same response type (allogrooming-responsive or sniffing-responsive) and distribution based on shuffled data in which the response type is randomly permuted (100 rounds of shuffling). **f**, Example calcium traces from single neurons that show increased activity during self-grooming but not allogrooming or sniffing. **g**, Heatmaps showing average responses of example self-grooming-responsive cells (with either increased or decreased activity) centered around self-grooming onset. **h**, Fraction of cells activated during both self-grooming and allogrooming or during both self-grooming and sniffing. **i**, Example image showing retrograde labelling of neurons in the accessory olfactory bulb (AOB) by injecting a retrograde AAV-EGFP virus in the MeA. Scale bar, 200 µm. **c**, **d**, **g**, Time 0 indicates behavior onset. **e**, n = 338, 1560, and 189800 pairwise distances for allogrooming-encoding cells, sniffing-encoding cells, and cells with shuffled identity, respectively. Kolmogorov-Smirnov test. **h**, Hypergeometric test. ns, not significant. For details of statistical analyses, see Supplementary Table 1.

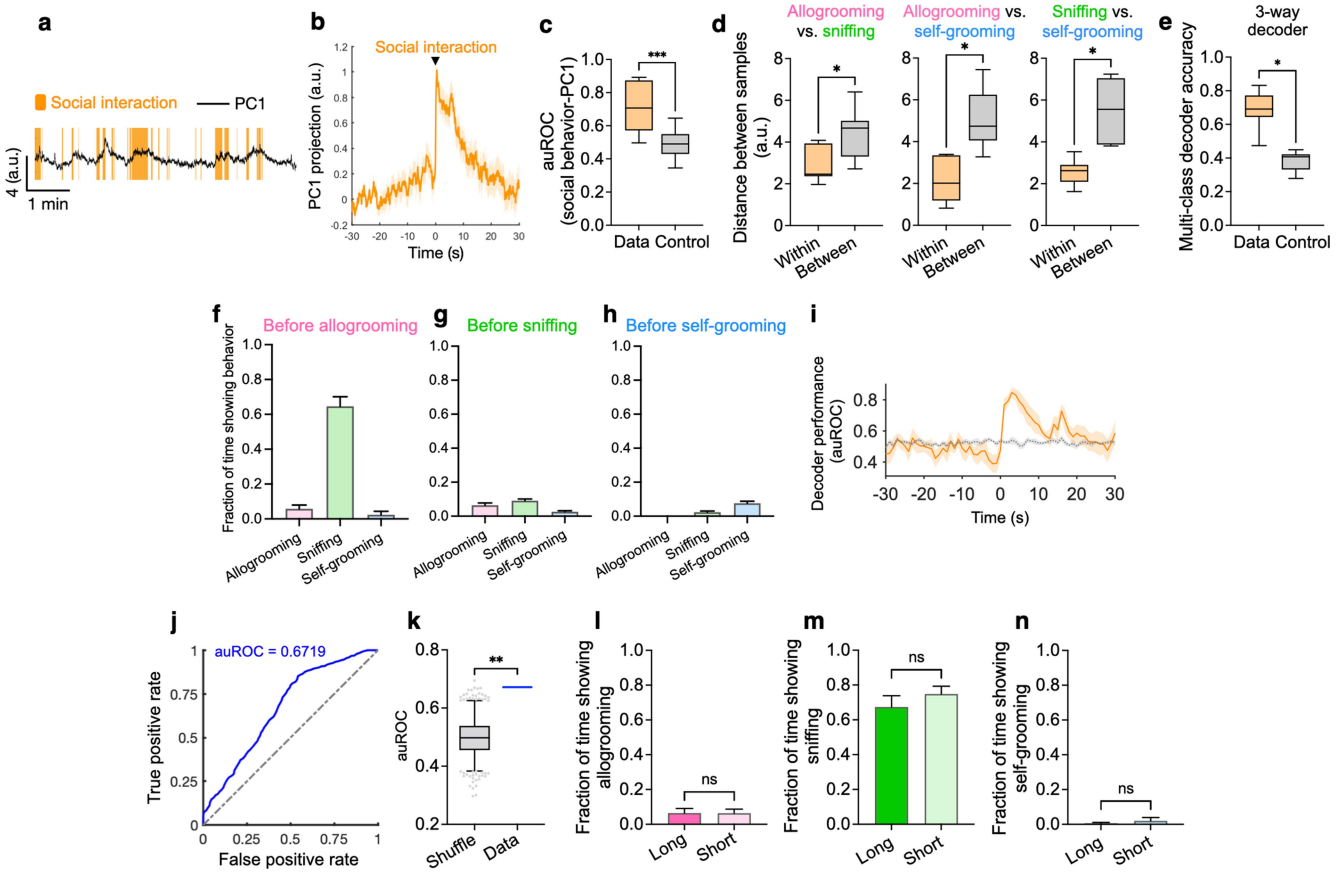

Extended Data Fig. 4 | MeA population activity encodes allogrooming and other behaviors during prosocial interaction. a, Projection of MeA population activity onto the first principal component (PC) overlaid with annotation of social interaction (including allogrooming and sniffing) in an example animal. **b**, Trial-averaged PC1 activity centered around onset of social interaction across all bouts from all sessions. **c**, Quantification of area under ROC curve (auROC) characterizing the relationship between PC1 activity and social interaction. **d**, Pairwise comparisons of the average within- and between-behavior class Euclidean distances (measured on the first 2 PCs within each session) for allogrooming vs. sniffing, allogrooming vs. self-grooming, and sniffing vs. self-grooming. **e**, Performance of three-way multi-class SVM decoders trained to predict allogrooming, sniffing, or self-grooming behavior. **f**–**h**, Fraction of time that subjects show different types of behaviors (allogrooming, sniffing, or self-grooming) during the 3 s prior to the onsets of allogrooming (**f**), sniffing (**g**), and self-grooming events (**h**). **i**, Time-course of behavior decoder performance in discriminating between allogrooming and sniffing centered around onset of behavior. Shuffle control decoders are constructed using time-permuted calcium traces. Note that although a fraction of allogrooming events were preceded by sniffing events (**f**), the performance of the decoder remains at chance level prior to the onset of behavior (**i**), suggesting that neural activity during preceding sniffing events is not sufficient to decode allogrooming vs. sniffing. **j**, ROC curve quantifying performance of a binary decoder to predict whether an allogrooming bout is short (≤ 5s) or long (> 5s) using population activity centered around onset of allogrooming. **k**, Decoder performance in (**j**) compared with a null distribution constructed using time-permuted calcium traces. Whiskers indicate the 2.5th and 97.5th percentiles of null distribution. Blue line: auROC from real data. **l**–**n**, Fraction of time that subjects show allogrooming (**l**), sniffing (**m**), or self-grooming (**n**) during the 3 s prior to the onsets of long or short allogrooming events. Mean ± s.e.m. The ability to predict allogrooming bout duration using population activity is unlikely to be attributable to differences in behaviors preceding allogrooming as there is no difference in the distribution of different behaviors prior to allogrooming onset between the long and short bouts. **b**, **i**, Time 0 indicates behavior onset. **b**, **f**–**i**, **l**–**n**, mean ± s.e.m. Boxplots: median with quartiles, 1.5 × IQR and outliers. **b**, $n = 7$ independent imaging sessions (from 6 subject mice). **c**, $n = 7$ independent imaging sessions (from 6 subject mice) and 70 rounds of shuffling (10 rounds for each imaging session) for control group. Two-sided Wilcoxon rank-sum test. **d**, **e**, $n = 7$ independent imaging sessions (from 6 subject animals). Two-sided Wilcoxon signed-rank test. **f**–**h**, $n = 51, 292, 223$ allogrooming (**f**), sniffing (**g**), and self-grooming (**h**) bouts, respectively (in 7 independent imaging sessions in 6 subject animals). **k**, permutation test (1000 rounds of permutation). **l**–**n**, $n = 51$ short and 38 long allogrooming bouts (from 7 independent imaging sessions in 6 subject animals). Two-sided Wilcoxon rank-sum test. ***$P < 0.001$, **$P < 0.01$, *$P < 0.05$. ns, not significant. For details of statistical analyses, see Supplementary Table 1.

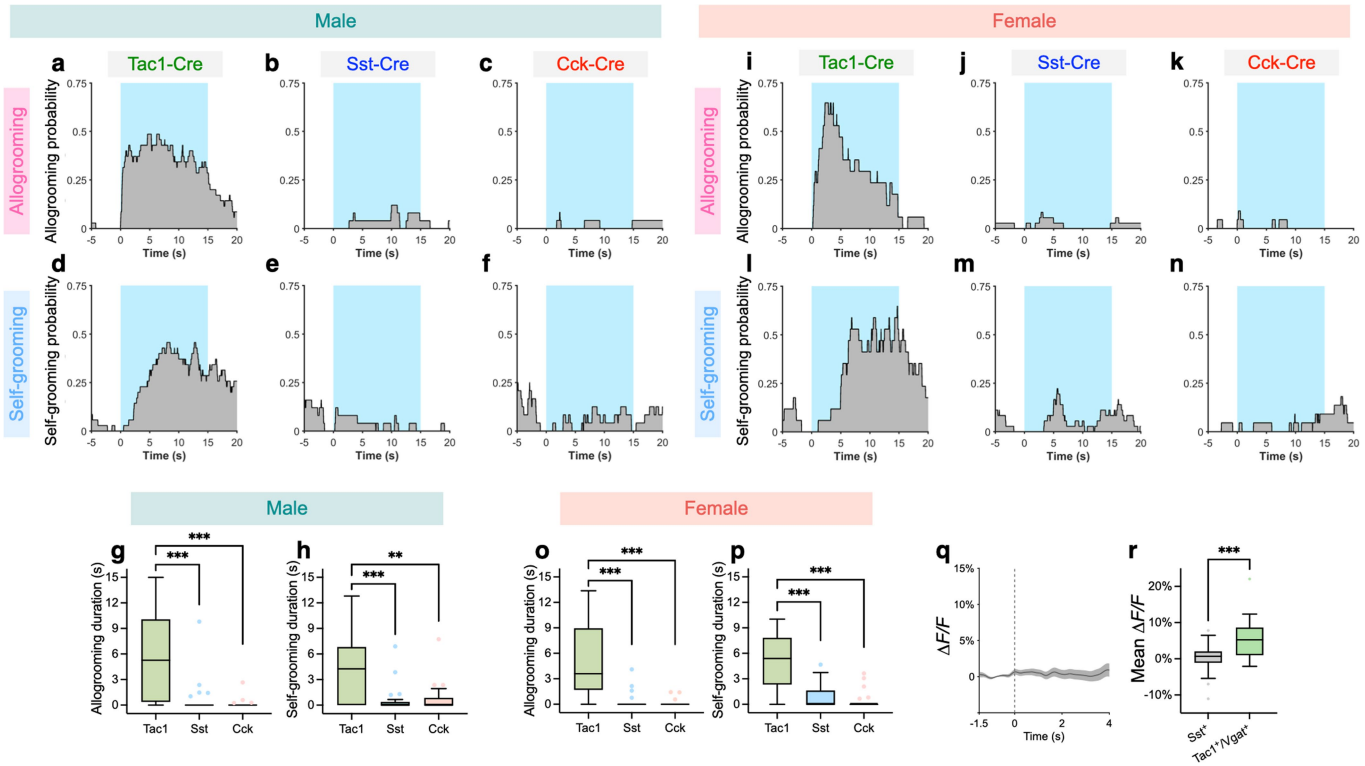

Extended Data Fig. 5 | Activation of MeA^{Tac1} neurons promotes allogrooming and self-grooming in males and females. **a**–**f**, **i**–**n**, Probability of allogrooming (**a**–**c**, **i**–**k**) and self-grooming (**d**–**f**, **l**–**n**) (fraction of trials showing a particular behavior at different time points) with respect to stimulation onset during optogenetic activation in male (**a**–**f**) and female (**i**–**n**) Tac1-Cre (**a**, **d**, **i**, **l**), Sst-Cre (**b**, **e**, **j**, **m**), and Cck-Cre (**c**, **f**, **k**, **n**) animals injected with ChR2 in the MeA. Blue areas: duration of light illumination; time 0: stimulation onset. **g**, **h**, **o**, **p**, Duration of allogrooming (**g**, **o**) and self-grooming (**h**, **p**) during photostimulations in male (**g**, **h**) and female (**o**, **p**) Tac1-Cre, Sst-Cre, and Cck-Cre animals injected with ChR2 in the MeA. **q**, Average trace showing Ca^{2+} signal changes during allogrooming toward stressed partners in Sst-Cre subjects expressing GCaMP. Mean ± s.e.m. Time 0: allogrooming onset. **r**, Comparison of Ca^{2+} signal changes between Sst$^+$ and Tac1$^+$/Vgat$^+$ neurons during allogrooming using mean $\Delta F/F$ after behavior onset. Boxplots: median with quartiles, 1.5 × IQR and outliers. **a**–**p**, Tac1-Cre, $n = 35$ trials in 2 males and 17 trials 2 females for both allogrooming and self-grooming. Sst-Cre, $n = 25$ trials in 2 males and 36 trials in 2 females for both allogrooming and self-grooming. Cck-Cre, $n = 24$ trials in 2 males and 22 trials in 2 females for both allogrooming and self-grooming. Kruskal-Wallis test followed by post hoc Dunn's multiple comparisons test. **r**, $n = 40$ bouts in 7 GCaMP animals for Sst$^+$ neurons. $n = 19$ bouts in 6 GCaMP animals for Tac1$^+$/Vgat$^+$ neurons. Data for Tac1$^+$/Vgat$^+$ neurons are the same as those in Fig. 4k and are presented here for comparison. Two-sided Wilcoxon rank-sum test. ***$P < 0.001$. **$P < 0.01$. For details of statistical analyses, see Supplementary Table 1.

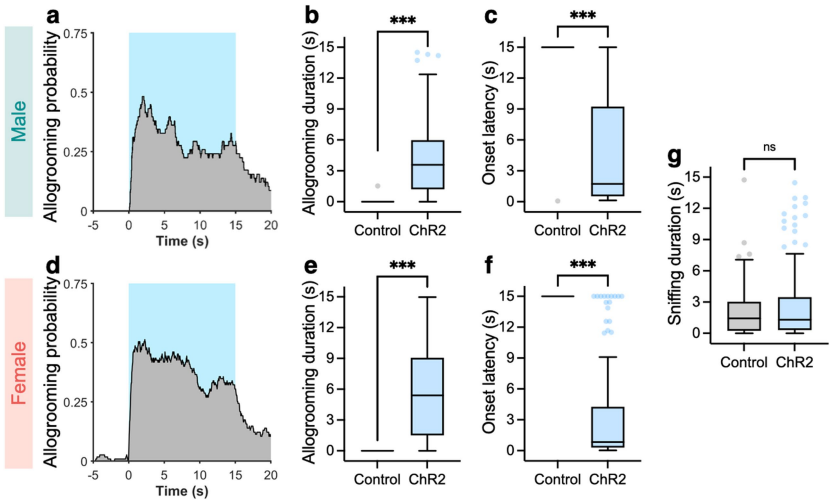

Extended Data Fig. 6 | Activation of MeA$^{Tac1\cap Vgat}$ neurons promotes affiliative allogrooming in males and females. a, **d**, Probability of allogrooming toward stressed partners (fraction of trials showing allogrooming at different time points) with respect to stimulation onset in male (**a**) and female (**d**) ChR2 animals. **b**, **c**, **e**, **f**, Boxplots of duration (**b**, **e**) and onset latency (**c**, **f**) of allogrooming during photostimulations in male (**b**, **c**) and female (**e**, **f**) eYFP control and ChR2 animals. **g**, No significant difference in the duration of sniffing during photostimulations between eYFP control and ChR2 animals. Blue areas: duration of light illumination; time 0: stimulation onset. eYFP control males, $n = 22$ trials in 2 mice. ChR2 males, $n = 58$ trials in 4 mice. eYFP control females, $n = 55$ trials in 4 mice. ChR2 females, $n = 115$ trials in 4 mice. In **g**, trials from males and females are combined. Boxplots: median with quartiles, 1.5 × IQR and outliers. Two-sided Wilcoxon rank-sum test. ***$P < 0.001$. ns, not significant. For details of statistical analyses, see Supplementary Table 1.

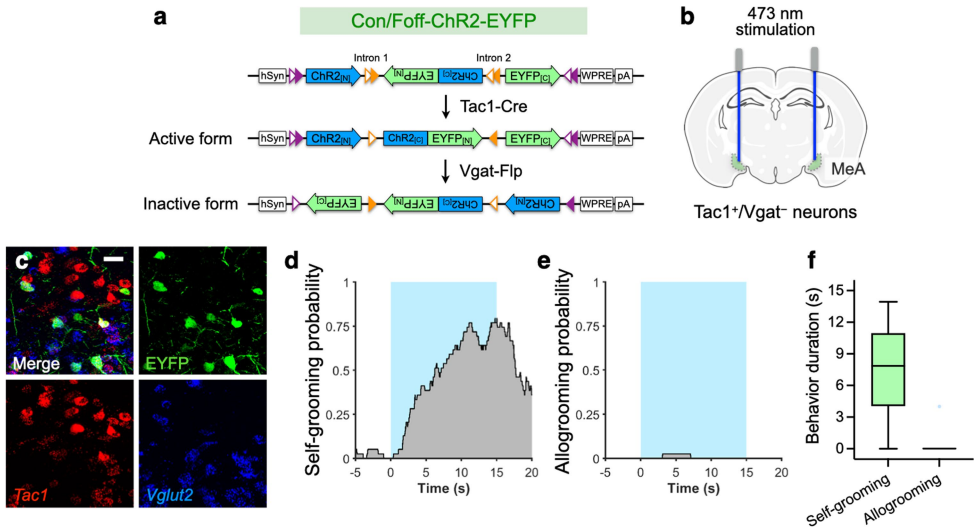

Extended Data Fig. 7 | Activation of MeA Tac1$^+$/Vgat$^-$ neurons promotes self-grooming but not allogrooming. a, **b**, Schematic of an intersectional approach for expression of ChR2 in Tac1$^+$/Vgat$^-$ neurons in the MeA using a Cre-on and Flp-off AAV virus. **c**, Example images showing that the majority of eYFP$^+$ cells are glutamatergic (Vglut2$^+$, 64.0 ± 1.8%, mean ± s.e.m.) and Tac1$^+$ (91.8 ± 0.5%, mean ± s.e.m.) in *Tac1*$^{cre/+}$/*Vgat*$^{flp/+}$ animals injected with the Con/Foff-eYFP virus (n = 3 hemispheres independently injected with the virus from 2 mice (5-7 sections per hemisphere). Scale bar, 25 µm. **d**, **e**, Probability of self-grooming (**d**) and allogrooming (**e**) toward stressed partners (fraction of trials showing a particular behavior at different time points) with respect to stimulation onset in ChR2 animals. Blue areas: duration of light illumination; time 0: stimulation onset. **f**, Duration of self-grooming and allogrooming toward stressed partners during photostimulations. Boxplots: median with quartiles, 1.5 × IQR and outliers. **d**–**f**, n = 39 trials in 4 mice (18 trials in 2 females and 21 trials in 2 males) for both self-grooming and allogrooming. The Cre-on/Flp-off virus used in the current study has been reported to lead to residual expression in a minor fraction of Cre$^+$/Flp$^+$ cells, possibly due to insufficiency of Flp relative to Cre (refs. [26,52]). Nonetheless, we found that when using this virus, the majority of eYFP$^+$ cells (64.0 ± 1.8%, mean ± s.e.m.) were Vglut2$^+$. Of note, the observation that the Cre-on/Flp-off animals did not show induction of allogrooming behavior suggests that activation of the small fraction of Tac1$^+$/Vgat$^+$ neurons in these animals (concurrent with activation of Tac1$^+$/Vgat$^-$ neurons) was not sufficient to drive allogrooming behavior. On the other hand, the observation that activation of Tac1$^+$/Vgat$^+$ neurons in animals injected with the Cre-on/Flp-on virus did not trigger self-grooming behavior suggests that the residual Tac1$^+$/Vgat$^+$ neurons labelled with the Cre-on/Flp-off virus are not responsible for the induction of self-grooming.

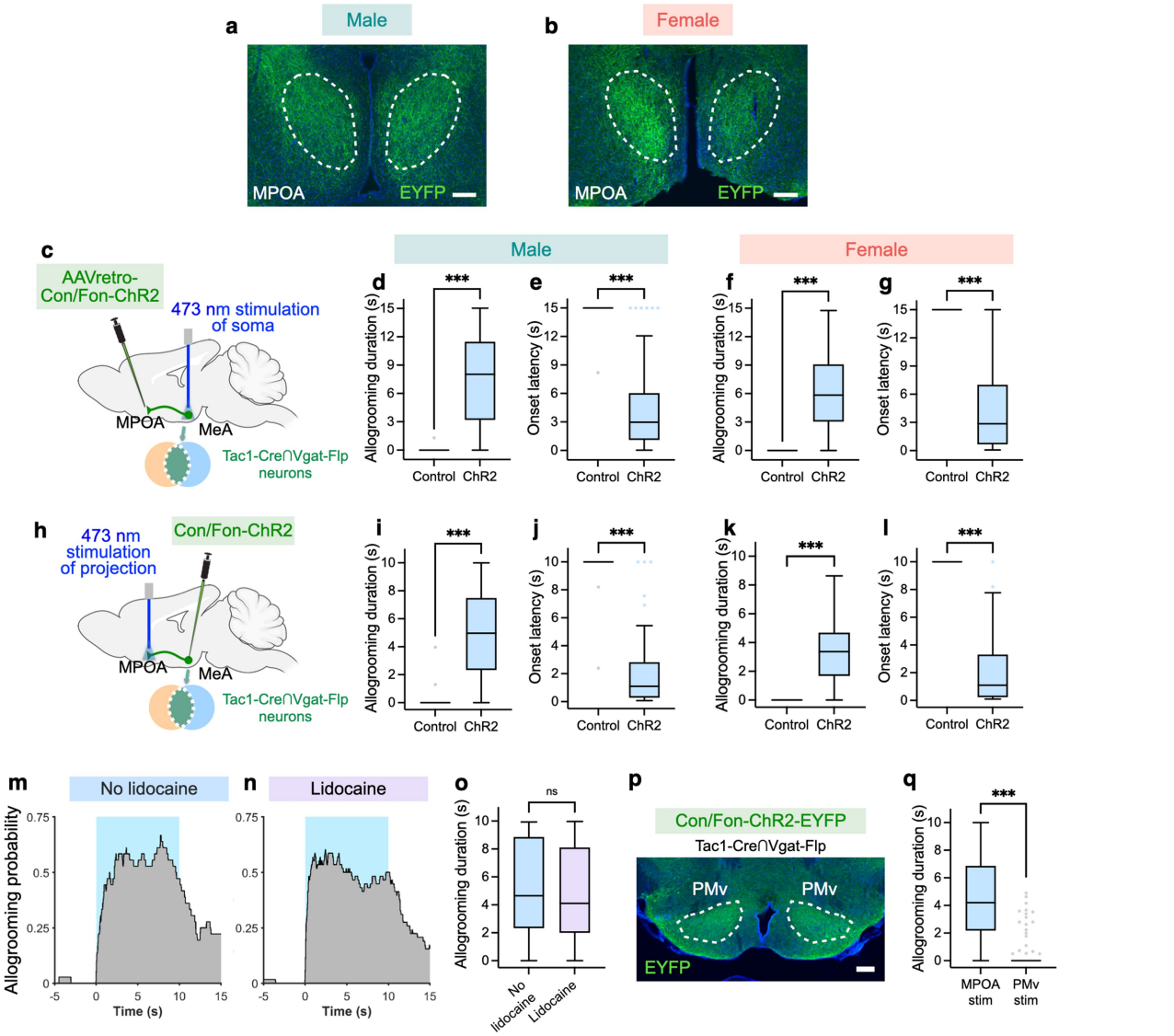

Extended Data Fig. 8 | MPOA-projecting MeA$^{Tac1\cap Vgat}$ neurons drive affiliative allogrooming in males and females. a, **b**, Example images showing axonal terminals of MeA$^{Tac1\cap Vgat}$ neurons in the MPOA in male (**a**) and female (**b**) animals, revealed by immunostaining for eYFP in *Tac1*$^{cre/+}$/*Vgat*$^{flp/+}$ animals injected with Con/Fon-ChR2-eYFP. Scale bar, 200 µm. (**c**, **h**) Schematics of viral injection and fibre implantation strategies for soma stimulation of retrogradely labelled, MPOA-projecting MeA$^{Tac1\cap Vgat}$ neurons (**c**) or stimulation of the axonal projection of MeA$^{Tac1\cap Vgat}$ neurons in the MPOA (**h**). **d**–**g**, Duration (**d**, **f**) and onset latency (**e**, **g**) of allogrooming during photostimulations in eYFP control and ChR2 males (**d**, **e**) and females (**f**, **g**) with soma stimulation of MPOA-projecting MeA$^{Tac1\cap Vgat}$ neurons. **i**–**l**, Duration (**i**, **k**) and onset latency (**j**, **l**) of allogrooming during photostimulations in eYFP control and ChR2 males (**i**, **j**) and females (**k**, **l**) with stimulation of the MPOA projection of MeA$^{Tac1\cap Vgat}$ neurons. **m**–**o**, Probability of allogrooming toward stressed partners (fraction of trials showing allogrooming at different time points) with respect to stimulation onset (**m**, **n**) and allogrooming duration (**o**) during photostimulations of the MPOA projection of MeA$^{Tac1\cap Vgat}$ neurons without or with infusion of lidocaine in the MeA. Blue areas: duration of light illumination; time 0: stimulation onset. **p**, Example image showing axonal projections of MeA$^{Tac1\cap Vgat}$ neurons in the PMv. Scale bar, 200 µm. **q**, Duration of allogrooming during photostimulation of the MPOA or PMv projection of MeA$^{Tac1\cap Vgat}$ neurons. Data for MPOA projection stimulation are the same as those in Fig. 4r and are presented here for comparison. Boxplots: median with quartiles, 1.5 × IQR and outliers. **d**–**g**, **i**–**l**, eYFP control, MeA soma stimulation, $n = 52$ trials in 4 females and 29 trials in 2 males. ChR2, MeA soma stimulation, $n = 68$ trials in 4 females and 59 trials in 2 males. eYFP control, MPOA projection stimulation, $n = 45$ trials in 4 females and 22 trials in 2 males. ChR2, MPOA projection stimulation, $n = 40$ trials in 3 females and 53 trials in 3 males. **m**–**o**, $n = 36$ trials in 4 mice (24 trials from 3 females and 12 trials from 1 male) for the "no lidocaine" group. $n = 58$ trials in 4 mice (39 trials from 3 females and 19 trials from 1 male) for the "lidocaine" group. **q**, $n = 93$ trials in 6 mice (40 trials in 3 females and 53 trials in 3 males) for MPOA stimulation, $n = 118$ trials in 4 mice (65 trials in 2 females and 53 trials in 2 males) for PMv stimulation. Two-sided Wilcoxon rank-sum test. ***$P < 0.001$. ns, not significant. For details of statistical analyses, see Supplementary Table 1.

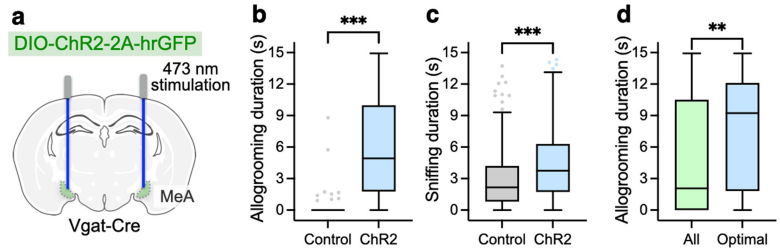

Extended Data Fig. 9 | Activation of MeA^{Vgat} neurons can promote allogrooming during prosocial interaction. a, Schematic of ChR2 activation in MeA^{Vgat} neurons. **b**, **c**, Duration of allogrooming (**b**) and sniffing (**c**) toward stressed partners during low-intensity photostimulations in ChR2 and eYFP control animals. The increase in sniffing (~1.5 s) appears to be substantially smaller than that in allogrooming (~5 s), suggesting that increased allogrooming is the predominant behavioral effect. **d**, Duration of triggered allogrooming when subject animals are in the vicinity of and attending to the partners ("optimal" condition) compared to all stimulations. Boxplots: median with quartiles, 1.5 × IQR and outliers. **b**, eYFP control, $n = 119$ trials in 11 mice (74 trials in 6 females and 45 trials in 5 males); ChR2, $n = 141$ trials in 12 mice (88 trials in 7 females and 53 trials in 5 males). **c**, eYFP control, $n = 119$ trials in 11 mice (74 trials in 6 females and 45 trials in 5 males); ChR2, $n = 142$ trials in 12 mice (89 trials in 7 females and 53 trials in 5 males). **d**, All condition, $n = 78$ trials in 5 male mice; optimal condition (subject within half a body-length and facing the partner), $n = 53$ trials in 5 male mice. **b**–**d**, Two-sided Wilcoxon rank-sum test. $^{***}P < 0.001$, $^{**}P < 0.01$. For details of statistical analyses, see Supplementary Table 1.

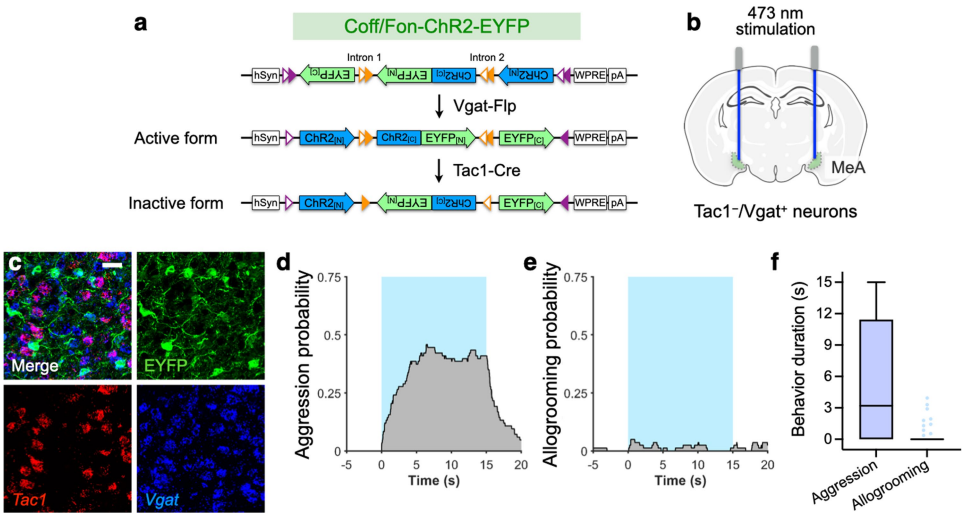

Extended Data Fig. 10 | Activation of MeA Tac1⁻/Vgat⁺ neurons promotes aggression. a–**b**, Schematic of an intersectional approach for specific expression of ChR2 in Tac1⁻/Vgat⁺ neurons in the MeA using a Cre-off and Flp-on AAV. **c**, Example images showing that eYFP⁺ cells are predominantly Vgat⁺ (99.3 ± 1.4%, mean ± s.e.m.) and Tac1⁻ (90.1 ± 1.9%, mean ± s.e.m.) in *Tac1*$^{cre/+}$/*Vgat*$^{flp/+}$ animals injected with the Coff/Fon-eYFP AAV ($n = 4$ hemispheres independently injected with the virus from 2 mice (4-5 sections per hemisphere). Scale bar, 25 µm. **d**, **e**, Probability of aggression (**d**) and allogrooming (**e**) toward stressed partners (fraction of trials showing a particular behavior at different time points) with respect to stimulation onset in ChR2 animals. Blue areas: duration of light illumination; time 0: stimulation onset. **f**, Duration of aggression and allogrooming toward stressed partners during photostimulations. Boxplots: median with quartiles, 1.5 × IQR and outliers. **d**–**f**, $n = 83$ and 80 trials in 4 male mice for aggression and allogrooming, respectively.

nature research

Corresponding author(s): Weizhe Hong

Last updated by author(s): Jul 28, 2021

Reporting Summary

Nature Research wishes to improve the reproducibility of the work that we publish. This form provides structure for consistency and transparency in reporting. For further information on Nature Research policies, see our Editorial Policies and the Editorial Policy Checklist.

Statistics

For all statistical analyses, confirm that the following items are present in the figure legend, table legend, main text, or Methods section.

n/a	Confirmed	
☐	☒	The exact sample size (*n*) for each experimental group/condition, given as a discrete number and unit of measurement
☐	☒	A statement on whether measurements were taken from distinct samples or whether the same sample was measured repeatedly
☐	☒	The statistical test(s) used AND whether they are one- or two-sided *Only common tests should be described solely by name; describe more complex techniques in the Methods section.*
☐	☒	A description of all covariates tested
☐	☒	A description of any assumptions or corrections, such as tests of normality and adjustment for multiple comparisons
☐	☒	A full description of the statistical parameters including central tendency (e.g. means) or other basic estimates (e.g. regression coefficient) AND variation (e.g. standard deviation) or associated estimates of uncertainty (e.g. confidence intervals)
☐	☒	For null hypothesis testing, the test statistic (e.g. *F*, *t*, *r*) with confidence intervals, effect sizes, degrees of freedom and *P* value noted *Give P values as exact values whenever suitable.*
☒	☐	For Bayesian analysis, information on the choice of priors and Markov chain Monte Carlo settings
☒	☐	For hierarchical and complex designs, identification of the appropriate level for tests and full reporting of outcomes
☐	☒	Estimates of effect sizes (e.g. Cohen's *d*, Pearson's *r*), indicating how they were calculated

Our web collection on statistics for biologists contains articles on many of the points above.

Software and code

Policy information about availability of computer code

Data collection	Microendoscopic imaging data was collected using an open source data acquisition software (https://github.com/Aharoni-Lab/Miniscope-DAQ-QT-Software). Fiber photometry data was collected using the Spike2 software (v10.09a).
Data analysis	Statistical analysis was conducted using Prism (v9, GraphPad), MATLAB (R2018a and R2019b, MathWorks), R (v3.4.3), and Python (v3.5.6). Code for behavioral analysis (https://github.com/pdollar/toolbox) and microendoscopic imaging data analysis (https://github.com/etterguillaume/MiniscopeAnalysis, https://github.com/zhoupc/CNMF_E, and https://github.com/flatironinstitute/NoRMCorre) is available on GitHub. Animal pose tracking was performed using SLEAP (https://github.com/murthylab/sleap/releases/tag/v1.0.9). The pre-trained Google Inception v3 network is available at https://download.tensorflow.org/models/image/imagenet/inception-2015-12-05.tgz. Deep neural network training was performed using TensorFlow 1.11.

For manuscripts utilizing custom algorithms or software that are central to the research but not yet described in published literature, software must be made available to editors and reviewers. We strongly encourage code deposition in a community repository (e.g. GitHub). See the Nature Research guidelines for submitting code & software for further information.

Data

Policy information about availability of data

All manuscripts must include a data availability statement. This statement should provide the following information, where applicable:

- Accession codes, unique identifiers, or web links for publicly available datasets
- A list of figures that have associated raw data
- A description of any restrictions on data availability

Source Data are provided for all figures. Additional data relating to the paper are available upon reasonable request to the corresponding author.

Field-specific reporting

Please select the one below that is the best fit for your research. If you are not sure, read the appropriate sections before making your selection.

☒ Life sciences ☐ Behavioural & social sciences ☐ Ecological, evolutionary & environmental sciences

For a reference copy of the document with all sections, see nature.com/documents/nr-reporting-summary-flat.pdf

Life sciences study design

All studies must disclose on these points even when the disclosure is negative.

Sample size	Sample sizes were not predetermined using statistical methods. Sample sizes were chosen to reliably measure experimental effects while minimizing the number of animals used in accordance with ethical guidelines. Our sample sizes are similar to those used in previous publications in the field (e.g. Burkett et al. 2016, Science; Allsop et al. 2018, Cell; Hu et al. 2021, Nat Neurosci), and are deemed appropriate based on the size and statistical significance of the effects and consistency across animals.
Data exclusions	In fiber photometry experiments, calcium signal was examined prior to behavioral procedures and animals showing very few calcium transients and a low signal-to-noise ratio were not used. Post hoc histological examination showed that viral injection and/or fiber-optic implantation missed the target region in these animals. Exclusion criteria were pre-established.
Replication	All behavioral, imaging, and optogenetics experiments were replicated in multiple animals with similar results (see Supplementary Table 1 for exact numbers of animals and/or trials for each experiment). Example micrographs were based on at least three independent biological samples (animals or independently injected brain hemispheres) showing similar results.
Randomization	Animals of appropriate genotype, sex, age, and weight were randomly assigned to experimental or control group.
Blinding	Experimenters were not blind to group allocation during data acquisition or analysis. We ensured that control and experimental groups were tested using the same experimental conditions (except for the experimental treatments or manipulations) whenever necessary, and that data from control and experimental groups were analyzed using the same criteria and methods.

Reporting for specific materials, systems and methods

We require information from authors about some types of materials, experimental systems and methods used in many studies. Here, indicate whether each material, system or method listed is relevant to your study. If you are not sure if a list item applies to your research, read the appropriate section before selecting a response.

Materials & experimental systems

n/a	Involved in the study
☐	☒ Antibodies
☒	☐ Eukaryotic cell lines
☒	☐ Palaeontology and archaeology
☐	☒ Animals and other organisms
☒	☐ Human research participants
☒	☐ Clinical data
☒	☐ Dual use research of concern

Methods

n/a	Involved in the study
☒	☐ ChIP-seq
☒	☐ Flow cytometry
☒	☐ MRI-based neuroimaging

Antibodies

Antibodies used	1. Rabbit anti-GFP antibody (Invitrogen, Catalog # A-11122) 2. Donkey anti-rabbit IgG secondary antibody (Invitrogen, Catalog # A-21206)
Validation	1. Rabbit anti-GFP antibody – Validation statement from vendor: "Antibody specificity was demonstrated by detection of different targets fused to GFP tag in transiently transfected lysates tested. Relative detection of GFP tag was observed across different proteins fused with GFP in H3-GFP (Lane 3-5) and p65-GFP (Lane 6). GFP-variant, YFP is also being detected in His-p65-YFP lysate (Lane 7)." This antibody has been cited in at least 527 publications for immunohistochemistry according to the vendor's website. 2. Donkey anti-rabbit IgG secondary antibody – This antibody has been cited in at least 74 publications for immunohistochemistry according to the vendor's website.

Animals and other organisms

Policy information about studies involving animals; ARRIVE guidelines recommended for reporting animal research

Laboratory animals	Mice strains used in this study include C57BL/6J, BALB/cJ, Vgat-Cre, Vgat-Flp, Tac1-Cre, Sst-Cre, and Cck-Cre. All strains were purchased from Jackson Laboratories (stock No: 000664, 000651, 028862, 029591, 021877, 013044, and 012706). Animals were

	housed in 12 h light-dark cycle (10 p.m. – 10 a.m. light), with food and water available ad libitum. The housing facility had a temperature of 21–23oC and a humidity of 30–70%. Both males and females were used for experiments. 12-16-week-old animals were used for characterization of prosocial interaction in wild-type animals. 10-12-week-old animals were used for stereotaxic surgeries and were tested in behavioral experiments after >4 weeks following surgeries.
Wild animals	No wild animals were used in this study.
Field-collected samples	No field-collected samples were used in this study.
Ethics oversight	Care and experimental manipulations of all animals were carried out in accordance with the NIH Guide for Care and Use of Laboratory Animals and approved by UCLA IACUC.

Note that full information on the approval of the study protocol must also be provided in the manuscript.